AGU100 ADVANCING EARTH AND SPACE SCIENCE

Geochemistry, Geophysics, Geosystems

RESEARCH ARTICLE
10.1029/2018GC007516

On the Scales of Dynamic Topography in Whole-Mantle Convection Models

M. Arnould[1,2], N. Coltice[3], N. Flament[4], V. Seigneur[5], and R. D. Müller[2]

[1]Université de Lyon, École Normale Supérieure de Lyon, Université Claude Bernard, Laboratoire de Géologie de Lyon, Terre, Planètes, Environnement, CNRS UMR 5276, 2 rue Raphaël Dubois, Villeurbanne, France, [2]EarthByte Group, School of Geosciences, Madsen Building F09, University of Sydney, Sydney, New South Wales, Australia, [3]Laboratoire de Géologie, École Normale Supérieure, CNRS UMR, PSL Research University, Paris, France, [4]School of Earth and Environmental Sciences, University of Wollongong, Wollongong, New South Wales, Australia, [5]École Normale Supérieure de Lyon, Unité de Mathématiques Pures et Appliquées, CNRS UMR 5669, 46 Allée d'Italie, Lyon, France

Key Points:
- We identify a parameter range for which 2-D mantle convection models produce Earth-like tectonics, plate velocities, heat flow, and topography
- In these models, dynamic topography is substantial at large, intermediate, and small spatial scales
- Feedbacks between mantle flow and lithosphere dynamics control the spatiotemporal distribution of dynamic topography

Correspondence to:
M. Arnould,
maelis.arnould@ens-lyon.fr

Citation:
Arnould, M., Coltice, N., Flament, N., Seigneur, V., & Müller, R. D. (2018). On the scales of dynamic topography in whole-mantle convection models. *Geochemistry, Geophysics, Geosystems*, *19*. https://doi.org/10.1029/2018GC007516

Received 1 MAR 2018
Accepted 31 JUL 2018
Accepted article online 14 AUG 2018

Abstract Mantle convection shapes Earth's surface by generating dynamic topography. Observational constraints and regional convection models suggest that surface topography could be sensitive to mantle flow for wavelengths as short as 1,000 and 250 km, respectively. At these spatial scales, surface processes including sedimentation and relative sea-level change occur on million-year timescales. However, time-dependent global mantle flow models do not predict small-scale dynamic topography yet. Here we present 2-D spherical annulus numerical models of mantle convection with large radial and lateral viscosity contrasts. We first identify the range of Rayleigh number, internal heat production rate and yield stress for which models generate plate-like behavior, surface heat flow, surface velocities, and topography distribution comparable to Earth's. These models produce both whole-mantle convection and small-scale convection in the upper mantle, which results in small-scale (<500 km) to large-scale (>10^4 km) dynamic topography, with a spectral power for intermediate scales (500 to 10^4 km) comparable to estimates of present-day residual topography. Timescales of convection and the associated dynamic topography vary from five to several hundreds of millions of years. For a Rayleigh number of 10^7, we investigate how lithosphere yield stress variations (10–50 MPa) and the presence of deep thermochemical heterogeneities favor small-scale (200–500 km) and intermediate-scale (500–10^4 km) dynamic topography by controlling the formation of small-scale convection and the number and distribution of subduction zones, respectively. The interplay between mantle convection and lithosphere dynamics generates a complex spatial and temporal pattern of dynamic topography consistent with constraints for Earth.

1. Introduction

Surface elevations result from both external and internal processes that continuously shape the Earth over a wide range of rhythms and scales. Mantle flow, by transporting temperature and density anomalies and deforming the surface, generates dynamic topography, a mechanism first proposed by Pekeris (1935).

Global models of mantle flow and density can be used to predict Earth's dynamic topography. Instantaneous mantle flow models usually include density anomalies deduced from seismic tomography models (e.g., Conrad & Husson, 2009; Hager et al., 1985; Steinberger, 2007), and these density anomalies can be backward advected back to ~75 Myr (Conrad & Gurnis, 2003). Some flow models use reconstructed surface plate velocities as a top boundary condition together with a *slab assimilation* technique in forward models (Bower et al., 2015) or adjoint methods to constrain both mantle flow and surface observables (Liu et al., 2008). Despite the different methods used, these studies attribute large-scale topography anomalies (wavelengths longer than 10^4 km) to whole-mantle convection (Hager & Richards, 1989; Ricard et al., 1993). For example, Lithgow-Bertelloni and Silver (1998) invoked large-scale whole-mantle upwelling flow to explain large topography anomalies such as the African superswell, and Mitrovica et al. (1989) showed that slabs sinking into the mantle could explain the formation of intracontinental sedimentary basins such as the Western Interior Seaway in North America. Large-scale dynamic topography in such settings is predicted to evolve at rates between less than 1 and 80 m/Myr (e.g., Flament et al., 2015).

Observational constraints require the existence of transient (<10 Myr) and localized (<3,000 km) dynamic topography. Pulses of mantle plume activity or upper mantle vigorous convection at a maximal rate of

~100 m/Myr could explain seismic and stratigraphic observations (Al-Hajri et al., 2009; Hartley et al., 2011). Interpretations of river drainage patterns in terms of continental margin uplift or subsidence (Pritchard et al., 2009; Roberts et al., 2012) or analyses of carbonate platforms (Czarnota et al., 2013) suggest surface uplift at rates between 75 and 400 m/Myr. Rowley et al. (2013) also suggested that dynamic topography changes at rates of up to 60 m/year over areas covering hundreds of kilometers could have been responsible for the uplift of the southeastern coast of the United States over the last 3 Ma. Regional models of dynamic topography and relative sea-level change associated with small-scale convection (Petersen et al., 2010) predict that surface topography is sensitive to mantle flow for wavelengths as short as 250 km and for timescales of the order of 2–20 Myr. Petersen et al. (2010) showed that small-scale convection could deflect the surface with an amplitude of about ±300 m and induce high-frequency (period 2–20 Myr) stratigraphic sequences of about 200-km wavelength. Moreover, analytical global models (Hager & Richards, 1989) suggest that dynamic topography should be particularly sensitive to upper-mantle density heterogeneities at short to intermediate wavelengths. A recent global model of present-day residual topography derived from seismic data collected worldwide, mainly at passive margins (Hoggard et al., 2016), confirms that the amplitude of residual topography is significant for wavelengths as short as ~1,000 km.

However, most global mantle convection models do not predict significant dynamic topography for wavelengths smaller than 5,000 km (Hoggard et al., 2016). Indeed, instantaneous flow models based on present-day tomography do not contain much density heterogeneity in the upper mantle due to the resolution of seismic tomography. In addition, the spatial variability of the seismic velocity to density conversion factor necessary to predict the mantle flow is uncertain and chemical effects are generally ignored in the uppermost mantle. Moreover, the effect of the uppermost mantle is often removed when calculating dynamic topography from global flow models to exclude lithospheric density anomalies that do not constitute dynamic topography (Flament et al., 2013; Lithgow-Bertelloni & Silver, 1998; Steinberger, 2007). Recently, Steinberger et al. (2017) showed that considering uppermost mantle density heterogeneities from a high-resolution near-surface tomography model, in combination with a global *S* wave model, produces intermediate scales of dynamic topography (500 to 10^4 km).

Here we use time-dependent convection models to explore the relationship between the spatiotemporal distribution of dynamic topography and the geodynamic processes from which it arises. We present 2-D spherical annulus models with large radial and lateral viscosity contrasts that generate both large-scale and small-scale convection and a plate-like behavior. We first vary the Rayleigh number, yield stress, and internal heat production rate to identify a range of models that generate plate-like behavior (Tackley, 2000) and produce surface heat flow, surface velocities, and topography distribution comparable to Earth's. In the selected models, the predicted dynamic topography, which we compute by subtracting the model isostatic topography from the total model topography, occurs both at small (<500 km) and large (>10^4 km) scales. This allows us to investigate the role of small-scale convection, subduction zones, large-scale mantle flow, and deep-seated thermochemical heterogeneities in controlling the patterns and timescales of dynamic topography evolution.

2. Methods

2.1. Two-Dimensional Convection Models With Self-Consistent Plate Generation

2.1.1. Governing Equations

We solved the following nondimensionalized equations (1) of mass, momentum, energy, and composition conservation in 2-D spherical annulus geometry, under the Boussinesq approximation for incompressible mantle flow (e.g., Ricard, 2015):

$$\begin{aligned} \boldsymbol{\nabla}\cdot\mathbf{v} &= 0, \\ \nabla p - \boldsymbol{\nabla}\cdot\left[\eta(\underline{\boldsymbol{\nabla}\mathbf{v}} + (\underline{\nabla\mathbf{v}})^T)\right] &= \mathrm{Ra}(\alpha(z)T + BC)\mathbf{e_r}, \\ \frac{\mathrm{D}T}{\mathrm{D}t} &= -\boldsymbol{\nabla}\cdot(\boldsymbol{\nabla}T) + H, \\ \frac{\mathrm{D}C}{\mathrm{D}t} &= 0, \end{aligned} \tag{1}$$

where $\mathbf{v}$ is the velocity vector; p, the dynamic pressure; η, the viscosity; T, the temperature; C, the composition (to represent continents and deep thermochemical piles); $\alpha(z)$, the depth-dependent thermal expansivity; H, the heat production rate; B, the chemical buoyancy ratio; and $\mathbf{e_r}$, the radial unit vector. $\mathrm{D}/\mathrm{D}t = \partial/\partial t + (\mathbf{v}\cdot\nabla)$

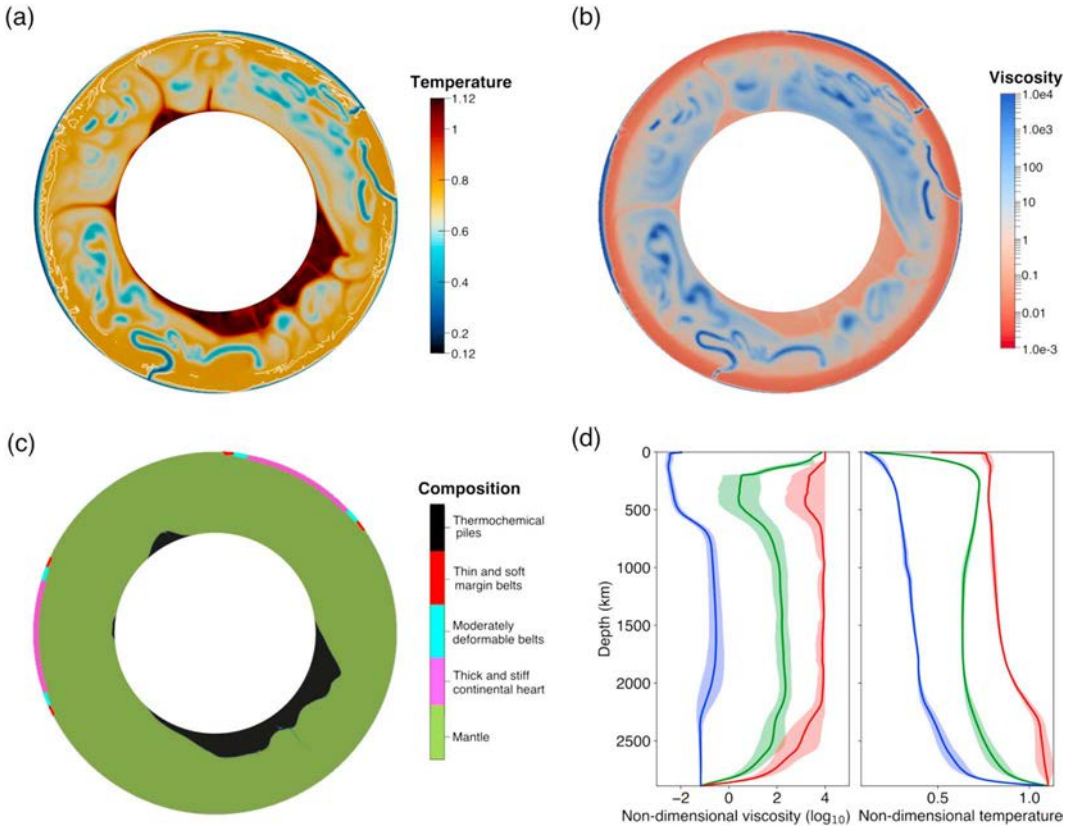

Figure 1. Snapshot of the nondimensional (a) temperature field with the 0.75 isotherm (corresponding to 1600 K) contoured in white in the upper mantle, (b) viscosity field, and (c) composition field for Model 1 with thermochemical continental rafts and deep piles. (d) Minimum (blue), mean (green), and maximum (red) viscosity and temperature profiles. Envelopes indicate temporal variations in viscosity and temperature. Note the maximum viscosity cutoff at 10^4.

is the Lagrangian time derivative. Ra is the Rayleigh number, defined as

$$\mathrm{Ra} = \frac{\alpha_0 g \Delta T \rho_0 h^3}{\eta_0 \kappa} \tag{2}$$

with α_0 the surface thermal expansivity; g, the gravitational acceleration; ΔT, the temperature drop across the mantle; ρ_0, the reference density; η_0, the reference viscosity; h, the thickness of the mantle; and κ, the reference thermal diffusivity. Using a Rayleigh number larger than 10^7 generates an Earth-like mantle vigor with an oceanic lithosphere of 150 km at most.

We used a depth-dependent thermal expansivity law obtained from Raman mode frequency shifts of Mg-SiO_3-perovskite in diamond-anvil-cell experiments and extrapolated to lower-mantle pressure and temperature range (Gillet et al., 2000). The resulting decrease in thermal expansivity by a factor of 3 with pressure (Chopelas & Boehler, 1992) broadens thermal anomalies in the deep mantle, stabilizes thermochemical heterogeneities (Hansen et al., 1993), and favors slab stagnation and hotter mantle plumes (Tosi et al., 2013). Even if depth-dependent thermal expansivity is inconsistent with the Boussinesq approximation, which states that mantle thermodynamic variables are independent on depth, it makes it possible to account for an extra source of buoyancy in the momentum equation, without the need of adding compressibility, viscous dissipation, and pressure-driven buoyancy force.

Viscosity depends exponentially on pressure and temperature following:

$$\eta(z,T) = \eta_0(z) \times \exp\left(A + \frac{E_a + \Pi(z)V_a}{RT}\right), \tag{3}$$

Table 1
Nondimensional and Dimensional Parameters

Parameter	Nondimensional value	Dimensional value
Surface temperature (T_{top})	0.12	255 K
Basal temperature (T_{bot})	1.12	2390 K
Mantle domain thickness (h)	1	2,890 km
Gravitational acceleration (g)	1	10 m/s^2
Reference thermal expansivity (α)	1	3×10^{-5} K^{-1}
Reference density (ρ_0)	1	4,400 kg/m^3
Reference diffusivity (κ)	1	1×10^{-6} m^2/s
Reference conductivity (k_0)	1	3.15 W·m^{-1}·K^{-1}
Viscosity constant (A)	−12.5	−88.75
Activation energy (E_a)	8	142 kJ/mol
Activation volume (V_a)	3	13.8 cm^3/mol
Maximum viscosity cutoff	10^4	10^{26} Pa·s
Viscosity increase at 660 km	30	
Yield stress gradient for all materials ($d\sigma_Y$)	2.34×10^6	1,088 Pa/m
Yield stress at the surface—continental interior ($\sigma_{Y_{cont}}$)	1×10^6	312 to 1.2×10^5 MPa
Viscosity increase—continental interior	1,000	
Buoyancy number—continental interior (B_{cont})	−0.41	−190 kg/m^3
Thickness—continental interior	0.0692	200 km
Yield stress at the surface—continental intermediate belt ($\sigma_{Y_{inter}}$)	4×10^5	125 to 5.1×10^4 MPa
Viscosity increase—continental intermediate belt	100	
Buoyancy number—continental intermediate belt (B_{inter})	−0.5	−235 kg/m^3
Thickness—continental intermediate belt	0.0432	125 km
Yield stress at the surface—continental margin belt ($\sigma_{Y_{marg}}$)	2×10^5	62.4 to 2.6×10^4 MPa
Viscosity increase—continental margin belt	10	
Buoyancy number—continental margin belt (B_{marg})	−0.6	−280 kg/m^3
Thickness—continental margin belt	0.0256	75 km
Buoyancy number—deep-seated thermochemical layer (B_{LLSVP})	0.25	117 kg/m^3
Initial thickness—deep-seated thermochemical layer	0.1038	300 km

Note. LLSVP = Large-low-shear-velocity province.

where A is chosen so that $\eta = \eta_0$ for $T = 0.64$ (which is the a priori temperature at the base of the lithosphere with dimensional value 1,600 K), E_a is the activation energy taken equal to 142 kJ/mol, which is the closest value to available constraints for Earth's activation energy (ranging between 300 and 600 kJ/mol; Hirth & Kohlstedt, 2003) that could be resolved numerically , $\Pi(z)$ is the static pressure, V_a is the activation volume, R is the gas constant, and T is the temperature; $\eta_0(z)$ is defined in order to ensure a viscosity jump by a factor of 30 at 660 km (d_0) over a depth $2d_{jump}$ of 100 km:

$$\eta_0(z) = \eta_{ref} \exp\left(\log(30)\left[1 - 0.5\left(1 - \tanh\left(\frac{d_0 - z}{d_{jump}}\right)\right)\right]\right), \quad (4)$$

where η_{ref} is the reference nondimensionalized viscosity value producing an average value of 1 for $\eta_0(z)$. The viscosity jump is suggested by geoid and postglacial rebound studies (Nakiboglu & Lambeck, 1980; Ricard et al., 1993). For computational reasons, we applied a maximum viscosity cutoff to limit the resulting viscosity variations to 7 orders of magnitude throughout the mantle domain (Figure 1). This is consistent with the study of King (2009), which showed that such a high value of the cutoff would produce topography errors <5%.

We used a pseudoplastic rheological law enabling strain localization (Tackley, 2000) based on the following yield stress threshold:

$$\sigma_Y = \sigma_Y + z \times d\sigma_Y, \quad (5)$$

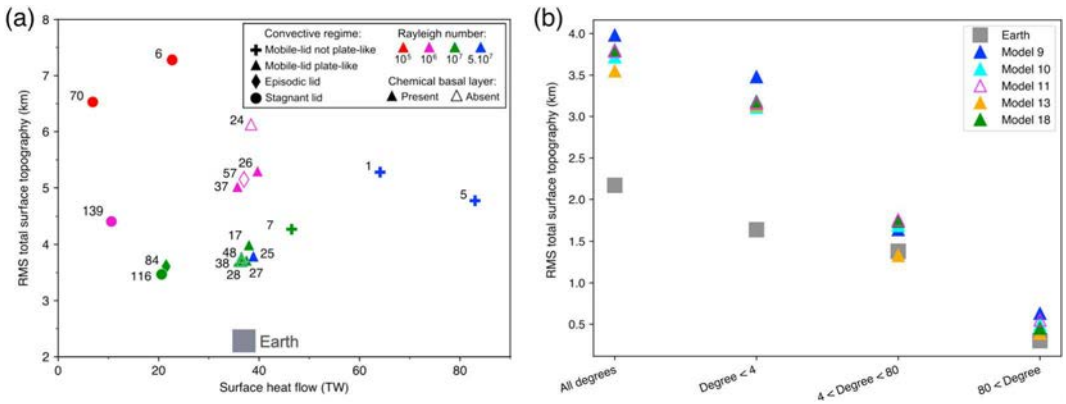

Figure 2. Regime diagram showing RMS total surface topography and surface heat flow for all models. Symbols describe the tectonic regime of each model. Empty and filled symbols represent models respectively excluding and including a chemical basal layer. Colors represent the reference Rayleigh number, and numbers correspond to the dimensional yield stress in megapascals. For comparison to the models, Earth's surface heat flow is without the radioactive contribution of the continental crust radioactivity (37–41 TW, Jaupart et al., 2007), and Earth's surface RMS total topography (about 2.17 km - Amante & Eakins, 2009) is modified to air loaded in the oceans. (b) Total and low-, band-, and high-pass-filtered RMS surface total topography for Earth and five models. RMS = root mean square.

where the value of the yield stress at the surface σ_Y is different for different materials and $d\sigma_Y$ is the yield stress depth derivative. When the yield stress σ_Y is reached, the viscosity η_Y drops markedly following:

$$\eta_Y = \frac{\sigma_Y}{2\dot{\epsilon}_{II}}, \tag{6}$$

where $\dot{\epsilon}_{II} = \sqrt{0.5\dot{\epsilon}_{ij}\dot{\epsilon}_{ij}}$, the second invariant of the strain rate tensor. This enables the localization of deformation (equation (6)) in order to mimic the dynamics of plate boundaries (e.g., Tackley, 2000) and seafloor area-age distribution (Coltice et al., 2012) at Earth's surface.

The range of values for parameters common to all presented models are listed in Table 1.

2.1.2. Model Setup

We computed a series of models (Figure 1) with the convection code StagYY (Tackley, 2000). The 2-D spherical annulus geometry makes it possible to compute mantle flow models that are comparable to 3-D spherical models without being computationally as expensive (Hernlund & Tackley, 2008). Free-slip conditions are used at both the core-mantle boundary and the surface. The lateral resolution is about 25 km at the surface and the radial resolution varies between 26 and 13 km due to a mesh refinement at boundaries.

We used 1.6×10^7 tracers and the tracer-ratio method (Tackley & King, 2003) to evaluate compositional fields. We set the initial thickness and excess density of the thermochemical layer (when considered) in order to obtain stable thermochemical piles through time following geodynamic laboratory (Davaille et al., 2003) and numerical (Deschamps & Tackley, 2009) studies. Although the thermal or thermochemical nature of large low-shear-velocity provinces is still debated (Garnero et al., 2016), we chose a maximum height of about 1,000 km above the core-mantle boundary for the volume of the basal layer, which is here considered chemically distinct, having a density excess of 3% compared to the ambient mantle. We considered two continental lithospheric rafts that are stiffer than oceanic lithosphere to remain stable throughout the time of integration (Lenardic & Moresi, 1999). They cover 30% of the surface area and are divided into three parts (Figure 1): cratons at the center, surrounded by proterozoic belts and mobile belts, in order of decreasing viscosity and density (see Table 1). We set decreasing density contrasts from continental interior to boundaries to compensate the effect of their decreasing thickness from interior to boundaries. This ensures that continents remain above the sea level throughout the time integration despite progressive dynamic erosion of their base. We first obtained an initial condition from the last step of a long equilibration phase in which all tracers are not advected (continents do not move and the basal thermochemical heterogeneity is a uniform layer). The initial state resulting from this equilibration phase is in statistical steady state for average mantle temperature and basal and surface heat flux. However, the fixity of continents during the equilibration phase leads to the presence of a transient initial hot area below continents, favored by their insulating effect (see Gurnis, 1993). This provides subcontinental positive buoyancy leading to elevated topography that decreases

Table 2
Model Input Parameters and Main Resulting Outputs

	Input parameters				Surface characteristics				Mantle properties		
Model	Ra	H (W/kg)	$\sigma_{Y_{oc}}$ (MPa)	CBL	P	M	Q_0 (TW)	h_{RMS} (km)	Q_0/Q_{CMB} (%)	T_{LAB}	η_0 (Pa·s)
Model 1	10^5	8.7×10^{-13}	6.37	Yes	0.13	0.16	22.7	7.28	6	0.78	1.1×10^{24}
Model 2	10^5	1.9×10^{-12}	70	Yes	0.94	0.97	6.9	6.53	19	0.72	1.2×10^{24}
Model 3	10^6	3.8×10^{-12}	139	Yes	0.88	0.47	10.6	4.41	25	0.72	1.2×10^{23}
Model 4	10^6	9.1×10^{-12}	26.2	Yes	0.86	1.01	39.7	5.30	7	0.76	1.1×10^{23}
Model 5	10^6	8.5×10^{-12}	24.8	No	0.91	1.13	38.4	6.13	7	0.80	1.0×10^{23}
Model 6	10^6	8.5×10^{-12}	37.1	Yes	0.93	0.93	35.7	5.02	8	0.80	1.0×10^{23}
Model 7	10^6	7.8×10^{-12}	57	No	0.97	0.86	37	5.15	8	0.86	9.5×10^{22}
Model 8	10^7	1.2×10^{-11}	7.42	Yes	0.88	1.15	46.4	4.27	8	0.68	1.2×10^{22}
Model 9	10^7	9.7×10^{-12}	16.9	Yes	0.93	0.97	38	3.98	10	0.74	1.2×10^{22}
Model 10	10^7	9.2×10^{-12}	27	Yes	0.97	0.85	37.5	3.72	9	0.75	1.1×10^{22}
Model 11	10^7	9.7×10^{-12}	28	No	0.95	1.03	36.5	3.79	15	0.71	1.2×10^{22}
Model 12	10^7	8.8×10^{-12}	38.2	Yes	0.97	0.88	35.9	3.70	8	0.78	1.1×10^{22}
Model 13	10^7	8.4×10^{-12}	48.8	Yes	0.96	0.80	36.5	3.55	9	0.81	1.0×10^{22}
Model 14	10^7	8.2×10^{-12}	84.3	Yes	0.92	0.60	21.5	3.61	20	0.82	1.0×10^{22}
Model 15	10^7	7.8×10^{-12}	116	Yes	−0.1	0.00	20.6	3.47	7	0.85	9.7×10^{21}
Model 16	5×10^7	9.2×10^{-12}	5.3	Yes	0.87	1.25	83	4.77	10	0.75	2.2×10^{21}
Model 17	5×10^7	1.4×10^{-11}	1.25	Yes	0.91	1.08	64.1	5.28	13	0.65	2.6×10^{21}
Model 18	5×10^7	9.7×10^{-12}	25	Yes	0.97	0.82	38.9	3.79	13	0.65	2.6×10^{21}
Earth	$\mathbf{10^{7.5}-10^9}$	$\mathbf{3-5\times10^{-12}}$[a]	**10–500**[b]	**??**	**>0.75**[c]	**??**	**37–41**[d]	**2.17**[e]	**17–35**[f]	**0.64**[g]	**??**

Note. *Ra* is the Rayleigh number as defined in equation (2); H, the internal heat production rate; CBL means chemical basal layer; $\sigma_{Y_{oc}}$ is the surface oceanic lithosphere yield stress; P, the plateness; M, the mobility; Q_0, the surface heat flow; h_{RMS}, the surface total RMS topography; Q_0/Q_{CMB}, the ratio of CMB to surface heat flow; T_{LAB}, the sublithospheric temperature; and η_0, the reference viscosity. ?? = Poorly-constrained parameters for Earth. The values in boldface highlight the parameter constraints for Earth.

[a]Present-day heat production rate deduced from the activity of radioactive elements K, U, and Th (Turcotte & Schubert, 2014). [b]Stress release from earthquakes (Allmann & Shearer, 2009) and high-pressure high-temperature experiments (Brace & Kohlstedt, 1980). [c]Earth's lowest bound plateness taken from f_{90} estimated by Kreemer et al., 2014 (2014; at least 14%). [d]Earth's total surface heat flow without continental lithosphere radioactive heat production (Jaupart et al., 2007). [e]RMS total topography of Earth from etopo1 (Amante & Eakins, 2009) after the removal of the loading of oceans. [f]After removal of continental crust heat production, according to Olson (2016). [g]Nondimensional sublithospheric temperature assuming the isotherm is 1600 K.

as continents start moving. Moreover, the existence of a basal chemical layer with a constant thickness promotes an initial uniform distribution of mantle plumes similar to models without basal thermochemical heterogeneities. Therefore, the self-consistent and progressive deformation of this basal layer leads to a progressive reorganization of mantle plumes into clusters over a period of about 200 Myr.

The initial condition resulting from this equilibration phase is in statistical steady state for average mantle temperature and basal and surface heat flux. We computed the thermochemical evolution with tracer advection over ~1,000 Myr, in order to compute statistics and observe a diversity of convective states. Although we used a 2-D geometry, each of these models is computationally expensive, because of the long time of integration, high resolution, and solving for large viscosity variations. The total computational time necessary for the 18 models presented in Figure 2a and Table 2 was about 775,000 CPU hours.

We computed a series of models to find the parameter range for which models present (1) plate-like behavior and (2) amplitudes of topography and surface heat flow comparable to observations (see Figure 2a and Table 2). We varied Ra between 10^5 and 5×10^7. Basal heating represents on average 6% to 25% of the total surface heat flux (Table 2), depending on the presence of a basal thermochemical layer. Most estimates of Earth's core heat flow range between 7 and 17 TW (Olson, 2016), which would represent >17% of Earth's total heat flow, excluding crustal radioactive heat production. Therefore, most of our models have a core heat flow lower than inferred for Earth. We also varied the dimensional value of the yield stress at room pressure between 1 and 140 MPa (Figure 2). These values are low compared to laboratory experiments on mantle rocks (Brace & Kohlstedt, 1980) and close to the stress drop of earthquakes (Allmann & Shearer, 2009). The pseudoplastic

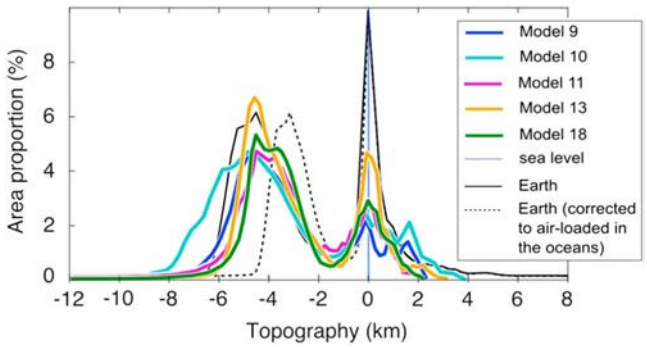

Figure 3. Time-averaged hypsometry for Models 9, 10, 11, 13, and 18 and Earth (etopo1 [Amante & Eakins, 2009], black solid line). The black dotted line is Earth's hypsometry corrected to air loaded in oceans.

rheology used here is empirical and probably represents homogenization of a variety of processes (including two-phase flow, grain size evolution, and damage) that occur at smaller spatial scales than resolved in our models. We found that larger yield stresses result in the formation of a stagnant lid at the surface of the domain (Figure 2a).

We determined models with plate-like behavior using the same diagnostics as Tackley (2000). We measured the plateness P as

$$P = 1 - \frac{f_{90}}{f_{90,\mathrm{iso}}}, \tag{7}$$

where f_{90} corresponds to the proportion of the surface localizing 90% of deformation and the value of $f_{90,\mathrm{iso}}$ is f_{90} for an isoviscous model; $f_{90,\mathrm{iso}}$ is about 0.6 for models with Ra $\geq 10^6$ and 0.54 for models with Ra $= 10^5$. An ideal plate tectonic layout gives $P = 1$. We also measured the mobility that is the ratio of the RMS surface velocity to RMS velocity in the whole domain. Plate-like behavior requires mobility close to or larger than 1. Among the models passing this test, we selected six models that displayed heat flow and total topography close to Earth's (see Figure 2a and Table 2). However, those models present a RMS total topography distribution about 1 km larger than Earth's for spherical harmonic degrees <4, while RMS total topography for degrees >4 matches Earth's intermediate and small wavelengths of RMS total topography (Figure 2b). This large-scale topography difference is caused by the overestimate of the density difference between continental and oceanic lithosphere in the models, as seen on the bimodal distribution of their surface topography (Figure 3), which is responsible for large-scale isostatic topography.

We focus on seven models. In Model 8 ($\sigma_Y = 7$ MPa), Model 9 ($\sigma_Y = 18$ MPa), Model 10 ($\sigma_Y = 27$ MPa), Model 13 ($\sigma_Y = 48$ MPa), and Model 14 ($\sigma_Y = 84$ MPa), Ra $= 10^7$ and a dense basal layer is included. In Model 11 ($\sigma_Y = 28$ MPa), Ra $= 10^7$ and a dense basal layer is not included. In Model 18 ($\sigma_Y = 25$ MPa), Ra $= 5 \times 10^7$ and a dense basal layer is included (Table 2). Models 9, 10, 11, 13, and 18 are characterized by a mobile-lid plate-like behavior. Model 8 is characterized by a mobile-lid but not plate-like convective regime. Model 14 is characterized by an episodic-lid convective regime. We consider these last two models to investigate the effect of different tectonic regimes on the spatial and temporal distribution of dynamic topography.

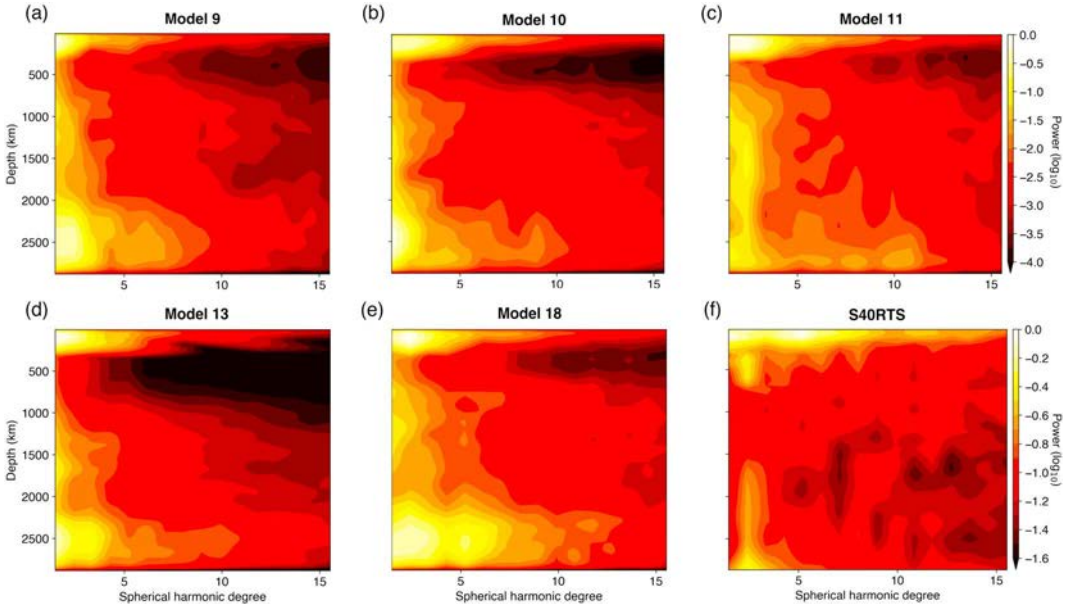

Figure 4. Temporal average of the thermal heterogeneity spectrum for (a) Model 9, (b) Model 10, (c) Model 11, (d) Model 13, and (e) Model 18 normalized by the highest power. (f) Shear wave velocity heterogeneity spectrum for seismic tomographic model S40RTS (Ritsema et al., 2011), also normalized by the highest power. The x axis ranges from spherical harmonic degree 1 to spherical harmonic degree 16.

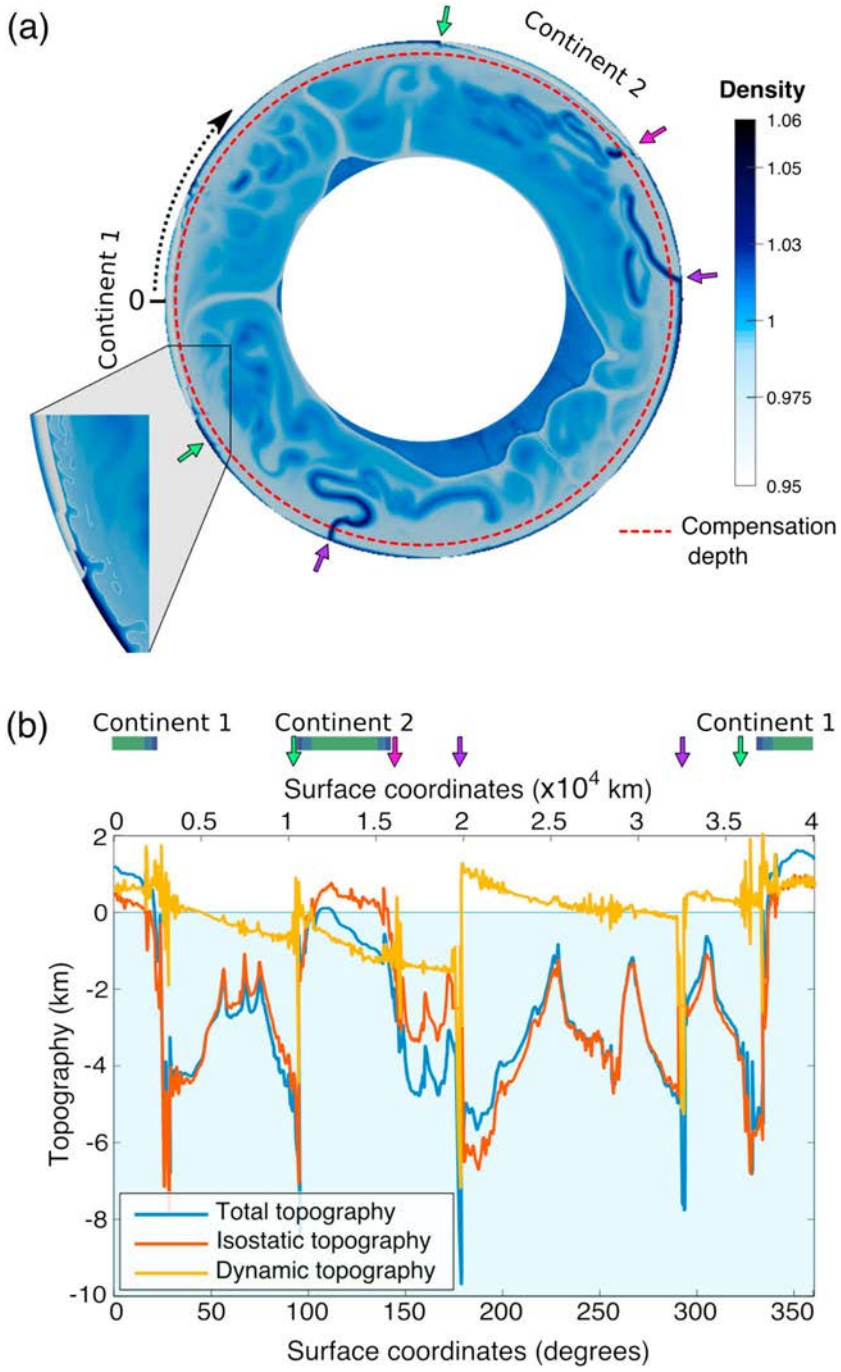

Figure 5. Total topography and its components for Model 10 for the same time step as in Figure 1. (a) Nondimensional mantle density field. The inset shows a close-up on small-scale convection, underlined by the white contour that represents the 0.75 nondimensional isotherm. (b) Dimensionalized surface total topography (blue) and isostatic (red) and dynamic (yellow) components. Surface coordinates increase clockwise from the left side of the spherical annulus surface, as shown by the black arrow on (a). Purple arrows show the locations of ongoing subduction zones, green arrows show the initiation position of future subduction zones, and the pink arrow shows a slab break-off event.

The time-averaged power spectra of temperature heterogeneities in the five plate-like models display strong low degrees, and a contribution from smaller scales in the shallow mantle (Figures 1a and 4), similar to seismic tomographic models such as S40RTS (Ritsema et al., 2011). This results from the large radial and lateral viscosity variations considered in our models (Coltice et al., 2017; Huang et al., 2003; Moresi & Solomatov, 1995; Solomatov & Moresi, 2000). Degree 1 is dominant in the lower mantle for the spectra of Models 9, 10, and 13. As the yield stress increases, less power is present at intermediate scales (degrees 5–16) in the upper mantle. In Model 11, the spectrum in the lower mantle is dominated by degree 2. The presence of thermochemical heterogeneities enhances the power of degrees smaller than 4. Increasing Ra breaks the degree 1 symmetry of the thermochemical layer and leads to strong amplitudes up to degree 7 in the lowermost mantle.

2.2. Computing Dynamic Topography

Many studies compute dynamic topography from the normal stresses arising from the convecting mantle, excluding the density anomalies located above a depth of 220 to 350 km from the flow calcuation, since the nonconvecting lithosphere extends down to these depths in some places (Flament et al., 2013; Lithgow-Bertelloni & Silver, 1998; Steinberger, 2007). Here we compute dynamic topography in a similar fashion to present-day residual topography (e.g., Gvirtzman et al., 2016), because our numerical solutions include small-scale convection near the lithosphere-asthenosphere boundary. We define dynamic topography as the vertical motion of the surface induced by mantle flow below the lithosphere (which is the upper conductive thermal boundary layer), in contrast to isostatic topography occurring above the lithosphere-asthenosphere boundary. We first calculate total topography from normal stresses at the surface σ_{zz} following:

$$h = \frac{\sigma_{zz}}{\rho g}, \tag{8}$$

where ρ is the density and g is the gravitational acceleration. The total topography predicted by the models averages to 0. In order to compare model topography and Earth's topography, we shift the total model topography by the average value of Earth's topography after removing water loading in the oceans. This value for a hydrosphere-free Earth is −2.3 km. We then calculate isostatic topography as the sum of all density contributions above a compensation depth, following the Airy condition (Figure 5a). Since dynamic topography averages to 0 to account for the conservation of the average radius of our models, and the total topography averages to −2.3 km by construction, isostatic topography also averages to −2.3 km. The compensation depth is taken as the inflection point of the average geotherm of the model at each time step and varies between 240- and 360-km depth depending on the temperature field. This method ensures that the modeled isostatic topography contains the density variations of both continental and oceanic lithospheres. We assume that the topography at subduction zones is completely dynamic since the Airy condition of pressure balance at the compensation depth cannot be satisfied there. We conservatively set isostatic topography to its average value within 500 km of subduction zones from the detection of their large negative normal velocity. This approach ensures that subduction topography is dynamic although the lateral extent of steeply dipping subduction zones is overestimated. We verify that increasing or decreasing the assumed lateral extent of subduction zones does not significantly affect the spatial distribution of dynamic topography. We obtain the dynamic component of topography by subtracting the isostatic topography from total topography.

On Figure 5b, we decomposed total topography (blue curve) into its isostatic (red curve) and dynamic (yellow curve) components for a snapshot of Model 10. The isostatic topography follows the shape of total topography, emphasizing its dominant role in the generation of topography (Gvirtzman et al., 2016). The amplitude of dynamic topography is ±2 km at most, except at subduction zones that we have considered to be entirely dynamic, hence reaching −7 km. The long-wavelength trend of dynamic topography (>10,000 km) is consistent with the longest wavelength of mantle convection, outlined by the location of large-scale density anomalies in the model at that time step (Figure 5a).

Depending on the geometry of slabs sinking in the mantle, dynamic topography around subduction zones is generally asymmetric within 5,000 km from trenches, being more negative above the dense sinking material, which generates downward radial stresses and velocities in the upper mantle (Figure 5b).

Short-wavelength (~200–500 km) dynamic topography variations that result from small-scale convection below the lithosphere (Figure 1) coincide with continents and old oceanic lithosphere (Figure 5b).

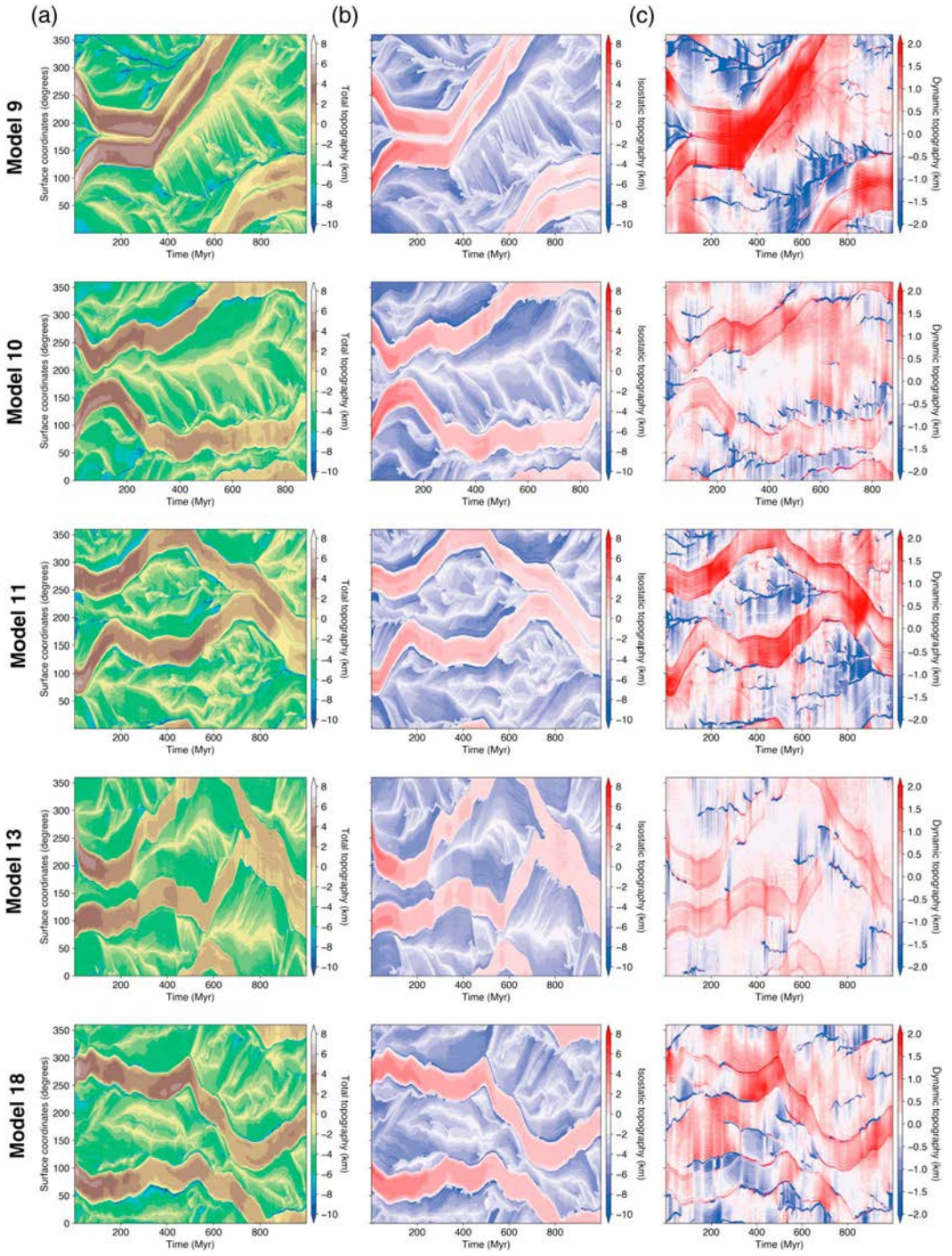

Figure 6. Temporal evolution of (a) total topography, (b) isostatic topography, and (c) dynamic topography for Models 9, 10, 11, 13, and 18. In (c), we limit the dynamic topography scale bar to ±2 km to enhance dynamic topography contrasts.

Small-scale dynamic topography is also caused by small-scale convection at continental boundaries (also called edge-driven convection) and by artificial excessive stresses at the boundaries between the different continental belts. These artifacts, caused by compositional differences between continental and oceanic lithosphere, do not affect our conclusions, as we do not focus on processes affecting continental margins. The description of this snapshot confirms that the predicted dynamic topography is directly linked to density anomalies advected within the mantle, as expected.

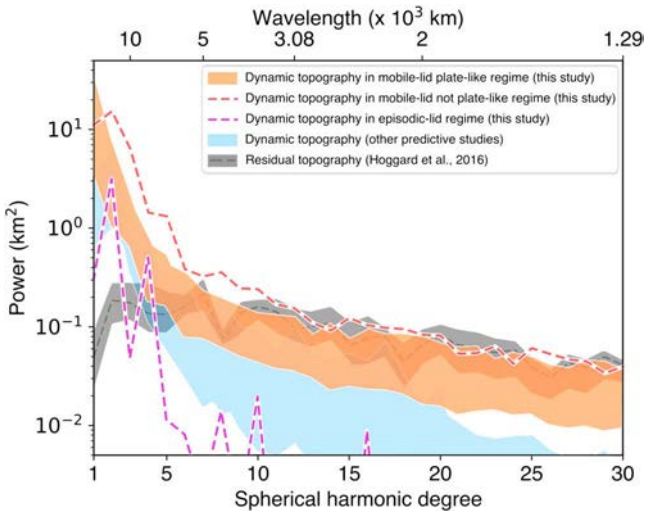

Figure 7. Temporal average of dynamic topography power spectra for Models 9, 10, 11, 13, and 18 with plate-like tectonics (orange-shaded area). Temporal average of dynamic topography power spectra for Model 8 in mobile-lid tectonic regime without plate-like tectonics (red dashed line) and Model 14 in episodic-lid regime (magenta dashed line). The predictive dynamic topography spectra of Conrad and Husson (2009), Flament et al. (2013), Ricard et al. (1993), Spasojevic and Gurnis (2012), and Steinberger (2007) are represented by the light blue envelope. The residual topography power spectrum obtained by regularized least squares inversion from Hoggard et al. (2016) is shown as a dashed gray line, with the gray envelope representing associated uncertainties.

3. Results

3.1. Spatial Distribution of Dynamic Topography

Figure 6 shows the evolution of total topography and its components through time for Models 9, 10, 11, 13, and 18. In Models 10 and 18, the two continents move freely and never collide, while in Models 9, 11, and 13, continents collide and form a supercontinent during the second half of the time integration. While supercontinent break-up is possible in principle, it was not observed in the time intervals considered. In all models, continental total topography decreases through time by about 1 km due to the combination of two phenomena. First, the presence of an initial hot area below continents, favored by their fixity during the equilibration phase and their insulating effect (see Gurnis, 1993), provides subcontinental positive buoyancy that decreases as continents start moving over 100 to 200 Myr. Continents present an average slightly positive (78 m in average) dynamic topography throughout the time integration of each model due to this insulation characteristic (Figure 6c). Second, the progressive basal erosion of continental lithosphere contributes to the decrease in their elevation through time, as shown by the decrease of isostatic topography on Figure 6b. This is a model effect that may not apply to Earth. Continents also get deflected downward at convergent margins.

In the oceanic domain, the total topography varies between ~ -1 and -15 km. The highest topographies correspond to ridges dynamically supported by plumes. The total elevation of other ridges is around -2 km. The lowest areas correspond to trenches. The elevation decreases continuously from ridges to trenches as expected on Earth. In our models, trenches and ridges last between ten and several hundreds of millions of years (Figures 6a and 6c). The average number of trenches decreases from about 15 to 1 as the yield stress increases from 7 to 84 MPa (Models 8, 9, 10, 13, and 14). The number of ridges evolves with that of trenches. As proposed by Mallard et al. (2016) for 3-D spherical models, the number and spatial distribution of plate boundaries vary with the yield stress for a given Rayleigh number in our models.

The spacing between trenches is rather even in Model 11, which is characterized by the absence of deep thermochemical heterogeneities. Keeping the same Rayleigh number and introducing thermochemical piles (Models 10 and 13), the spatial regularity is lost with subduction initiating closer to ocean-continent boundaries. Such models show a degree-1 dominant convection with a large-scale upwelling preferentially located below oceans. Increasing the Rayleigh number (Model 18) breaks the degree 1 and generates a more even spacing between trenches.

In Model 11, positive dynamic topography areas are about 1 km higher than in Model 10 because heat loss is more efficient in the absence of deep thermochemical piles. We verify that the presence of dense material

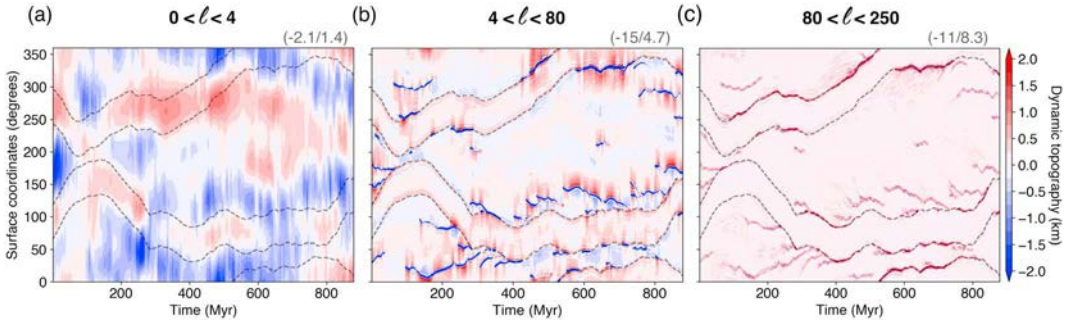

Figure 8. Low-pass, band-pass, and high-pass-filtered dynamic topography for Model 10. *l* is the spherical harmonic degree. Continent boundaries are delimitated with dashed lines. To enhance dynamic topography contrasts, we limit the dynamic topography scale bar to ±2 km. The minimum and maximum amplitudes of dynamic topography are annotated in parentheses.

at the base of the mantle in Model 10 opposes the positive buoyancy of ascending plumes and limits their vertical velocity. As a result, in Model 11, plumes are more positively buoyant and deflect the surface more than in Model 10. Model 18, for which the Rayleigh number is increased, also shows higher dynamic topography highs. Increasing the Rayleigh number with mixed heating decreases the average temperature below the boundary layer (Sotin & Labrosse, 1999). Therefore, plumes have a larger excess temperature and hence produce stronger dynamic topography.

Small-scale convection develops below old oceanic lithosphere and continents, as expected for Earth (Haxby & Weissel, 1986). As the number of subduction zones decreases, small-scale convection and small-scale dynamic topography are more developed since older and thicker oceanic lithosphere are present (Models 10 and 13). Model 8 (yield stress equal to 7 MPa) is characterized by the quasi-absence of small-scale topography, while small-scale topography is ubiquitous in Model 14 characterized by episodic-lid convection.

3.2. Spectral Decomposition of Dynamic Topography

We compute the spatial Fourier power spectrum of the average dynamic topography for Models 9, 10, 11, 13, and 18 in order to characterize the spatial distribution of dynamic topography power in plate-like regime, and for Models 8 and 14 that present different convective regimes. To compare these Fourier power spectra with existing 3-D spherical harmonics power spectra of global dynamic topography (e.g., Flament et al., 2013), we calculate and normalize the Fourier spectra for our models following the method described in Appendix A.

The power spectrum of dynamic topography in our models with plate-like tectonics (Figure 7) is characterized by a large power at low degrees (>1 km^2, for degrees 1 to 4) and a substantial power (> 2×10^{-2} km^2) for intermediate scales of dynamic topography (degrees 4–30). The average spectral power at degree 1 decreases from 10 km^2 for Model 11 (without thermochemical heterogeneities) to 4 km^2 for Model 10 (with thermochemical heterogeneities). At spherical harmonic degree 2, the average spectral power is 6 and 2.5 km^2 for Models 11 and 10, respectively. Basal thermochemical piles barely impact intermediate and small-scale dynamic topography. This decrease in amplitude of the largest scales of dynamic topography in Model 10 results from the fact that thermal buoyancy is partially compensated by the negative chemical buoyancy of basal thermochemical anomalies. Despite differences in the planform of convection between model cases (Figure 4), the power of dynamic topography is always predicted to be greater than 1 km^2 at low spherical harmonic degrees.

Increasing the yield stress from 7 to 84 MPa, while increasing the internal heating rate from 9×10^{-13} to 1×10^{-11} W/kg leads to a decrease in power at intermediate scales (from more than 10^{-1} km^2 for Model 8 to less than 10^{-3} km^2 for Model 14). Comparing the thermal heterogeneity spectra of Models 9, 10, and 13 (Figure 4), reveals that increasing the yield stress leads to a decrease in power at intermediate wavelengths (spherical harmonic degrees 4–16), particularly in the upper mantle since less subduction zones develop and the interior of the mantle heats up, prohibiting the rise of mantle plumes. Therefore, a larger part of topography is isostatic for a higher yield stress and the dynamic topography spectral power decreases.

While increasing the Rayleigh number from 10^7 (Model 10) to 5×10^7 (Model 18) modifies the spatial distribution of dynamic topography by imposing more vigorous convection (Figures 4 and 6), the average spectrum of dynamic topography from degree 1 to 40 is overall similar between these two models.

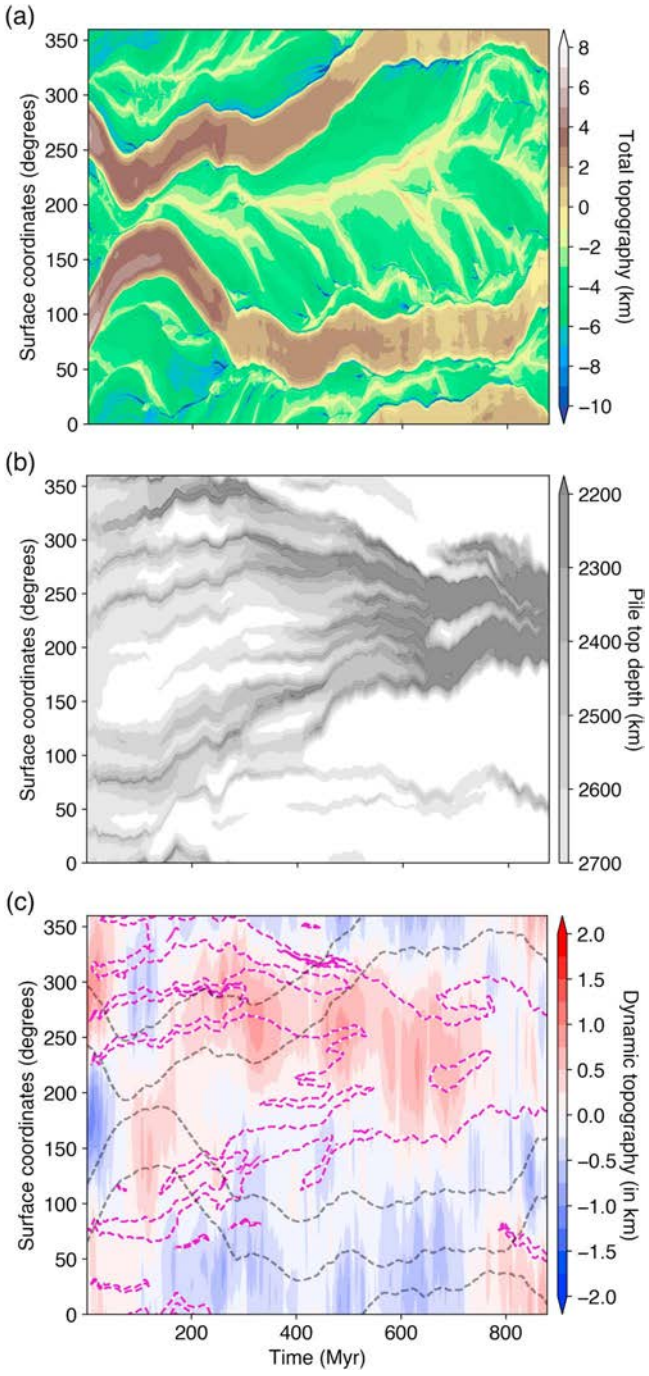

Figure 9. Temporal evolution of (a) total topography, (b) the depth of the top of thermochemical material, and (c) degree-2 low-pass-filtered dynamic topography for Model 10. In (c), continent boundaries are delimitated with gray dashed lines, and the 2,500-km pile depth contour is delimitated with magenta dashed lines. To enhance dynamic topography contrasts, we limit the dynamic topography scale bar to ±2 km.

In order to identify the sources of the different spectral signatures of dynamic topography, we used an order-5 Butterworth filter (Butterworth, 1930) to decompose the dynamic topography component of Model 10 (Figure 6c) into large (>5,000 km—spherical harmonic degree $l < 4$), intermediate (between 5,000 and 500 km—$4 < l < 80$) and small (<500 km—$l > 80$) scales (Figure 8). This filter has a flat response in the passband and a continuous slope decrease to the stopband frequency (no ripples), avoiding the addition of noise to the filtered signal.

In Model 10, large-scale dynamic topography highs (Figure 8a) have a maximum amplitude of 1.4 km. Figure 9 shows that dynamic topography highs are correlated with the position of large-scale upwellings, which are linked with the position of dense basal structures in Model 10. Large-scale dynamic topography lows (maximum amplitude −2.1 km) occur at subduction zones, which generally initiate on the sides of dense basal structures before moving toward continental edges. In other plate-like models, the maximum peak-to-peak amplitude is −3.1/2.3 km.

Filtering dynamic topography for intermediate scales (Figure 8b) shows that the main process controlling dynamic topography at these spatial scales is subduction. Slabs generally stagnate in the transition zone, which leads to changes in their dip angle. This is reflected in the temporal changes of the spatial distribution of dynamic topography amplitudes on either side of subduction zones. Continents are also affected by intermediate- to large-scale dynamic topography highs when plumes reach their base and spread laterally (Figure 8b).

Finally, all models displaying plate-like tectonics predict small-scale dynamic topography (Figure 8c), particularly developed below oceanic lithosphere near subduction zones, with an amplitude of ± 750 m at most and a wavelength of ~200 km. It is characterized by two viscous bulges surrounding a depression directly above the trench, as described in Husson et al. (2012). Small-scale convection below continental lithosphere produces dynamic topography wavelengths of about 500 km. This is larger scale than for the oceanic lithosphere, because continents are ten to a thousand times more viscous.

3.3. Temporal Evolution of Dynamic Topography

Large-scale mantle convection drives the temporal evolution of large-scale dynamic topography as highlighted by the superposition of the location of deep thermochemical heterogeneities, when present, and large-scale dynamic topography highs (Figure 9). The progressive self-organization of the basal thermochemical layer does not significantly affect the amplitude of large-scale dynamic topography (spherical harmonics of degrees 1 and 2, Figure 9c). In Models 9 and 11, the formation of a supercontinent is linked to an increase in the spectral power of dynamic topography at spherical harmonic degree 1. Such variations of large-scale dynamic topography occur on timescales of several hundreds of millions of years. In Model 13, this is not visible since one of the continents is surrounded by subduction zones, which generate a strong negative dynamic topography (Figure 6). Therefore, the spectral power associated to degree 1 is not as large as in Models 9 and 11 that are characterized by large-scale positive dynamic topography above continents at the time of the collision.

Intermediate scales of dynamic topography are also subjected to variations through time, in connection with the temporal evolution of the number of subduction zones. As shown on Figure 10, the spectral power of intermediate spherical harmonic degrees varies over time by about 1 order of magnitude for Models 9, 10, 11, 13, and 18. In Models 10 and 13, the decrease in the power of intermediate scales is associated with a decrease

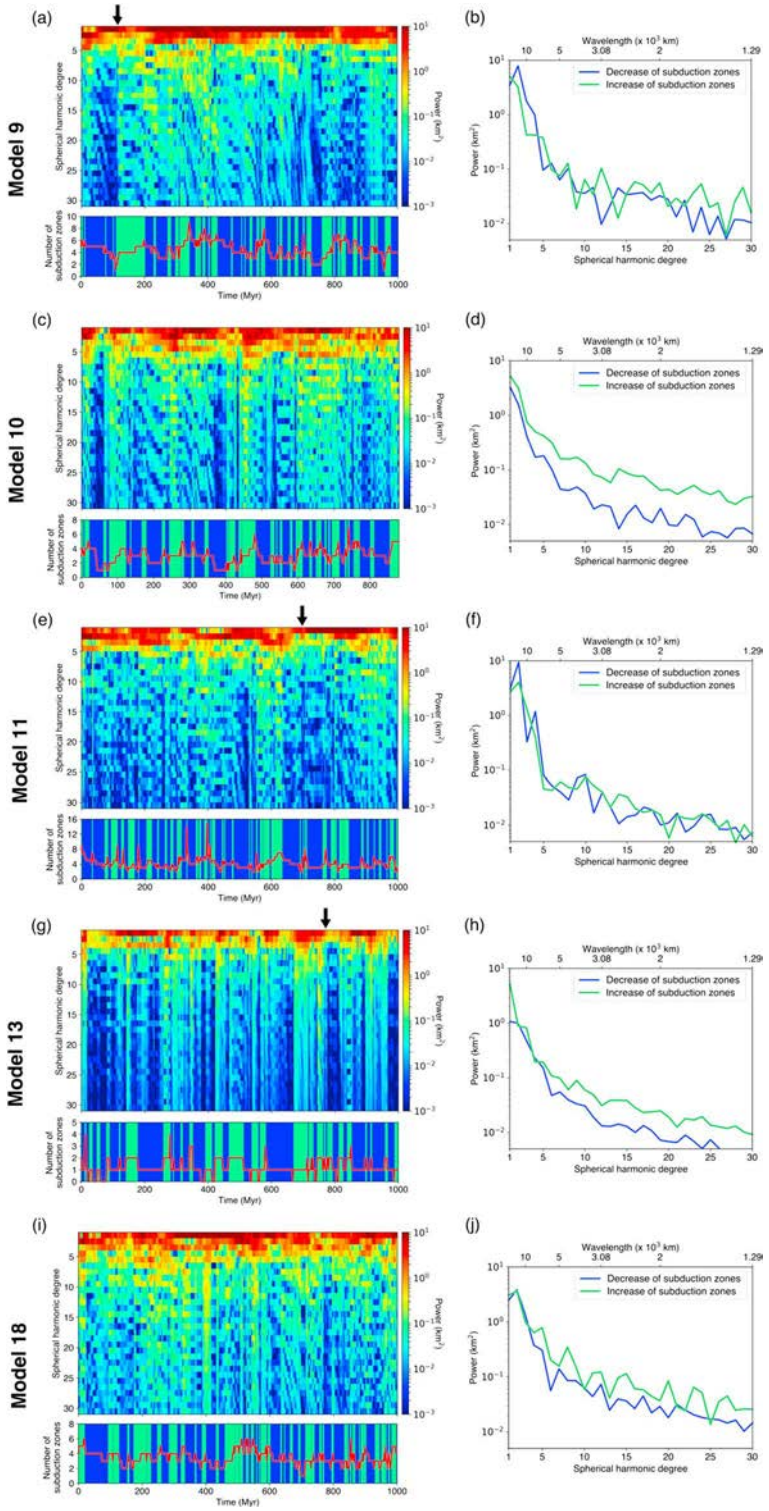

Figure 10. Temporal evolution of dynamic topography power spectrum and evolution of the number of subduction zones through time for Models 9 (a), 10 (c), 11 (e), 13 (g), and 18 (i). The blue zones are time intervals where the number of subduction zones decreases or has just decreased. The green regions show the time steps during which an increase in the number of subduction zones is observed or directly following an increase of the number of subduction zones. The black arrows indicate the formation of a supercontinent in Models 9, 11, and 13. Decomposition of the power spectra of dynamic topography for Models 9 (b), 10 (d), 11 (f), 13 (h), and 18 (j) according to the separation of spectra for the time steps following a decrease in the number of subduction zones (blue curve) and those following an increase in the number of subduction zones (green curve).

in the number of subduction zones (Figures 10d and 10h) whereas the initiation of subduction zones favors the development of intermediate wavelengths of dynamic topography. Such variations occur on timescales of about 50–100 Myr on average (Figures 10c and 10g). These timescales increase for increasing yield stress. In Models 10 and 13, a maximum of six subduction zones exist at any time. As a consequence, any subduction initiation or slab break-off event significantly modifies the spatial distribution of dynamic topography at intermediate wavelengths. In Models 9, 11, and 18, changes in the dynamic topography power spectrum at intermediate scales are less correlated with changes in the number of subduction zones. In Models 9 (low yield stress) and 11 (absence of dense basal heterogeneities), up to 15 subduction zones exist at any time, and they are distributed more homogeneously than in Models 10 and 13. Therefore, subduction initiation or slab break-off events have less impact on the spatial distribution of dynamic topography than in models with less subduction zones. Variations in the spectral power at intermediate scales can also be as frequent as every 10–50 Myr in Models 9, 11, and 18 than in Models 10 and 13 since subduction initiations and break-offs are more likely when the yield stress is lower than 20 MPa, in the absence of dense basal heterogeneities or for a Rayleigh number as high as 5×10^7. In Model 18, the large Rayleigh number leads to an homogeneous temporal distribution of subduction zones and relatively small changes in the temporal evolution of intermediate-scale dynamic topography as in Models 9 and 11.

The formation of a supercontinent in Models 9, 11, and 13 is associated with a strong decrease in the power at intermediate scales of dynamic topography. In Models 9 and 11, the decrease in dynamic topography power corresponds to subduction cessation due to continental collision. In Model 13, this decrease in the power spectrum of intermediate-scale dynamic topography occurs after the collision because a subduction zone persists at the margin of the newly formed supercontinent. Changes in the dip angle of subduction zones also regionally modify dynamic topography on timescales of several tens of millions of years (Figures 6 and 8b).

In all considered models, small-scale dynamic topography is linked to small-scale convection and subduction zones. Small-scale convection develops below moving plates and thus undergoes shearing deformation, which deflects the moving cells (Figure 1a). Short-lived cold droplets develop at the base of the lithosphere on timescales of the order of 1–10 Myr, thus deflecting the surface at this rhythm (Figure 8c). In the models, once the lithosphere has been shaped by small-scale convection, subsequent instabilities initiate at the same location, which leads to long-lived stationary waves of small-scale dynamic topography (timescale of the order of ~50–100 Myr, visible on Figure 8c) that only disappear when absorbed by a subduction zone. Local disturbances in the planform of small-scale convection are caused by the interplay between small-scale convection and rising plumes beneath oceanic lithosphere, which rejuvenate its base and temporarily erase small-scale convection in the direct vicinity of the plume conduit as described in Ballmer et al. (2011) and Coltice, Gérault, et al. (2017).

4. Discussion

4.1. Model Limitations

Because of the 2-D spherical annulus geometry of our models, temperature and density anomalies are still confined to a plane. Flow cannot propagate orthogonally to the 2-D plane and thus generates dynamic topography wavelengths longer than expected since the rising material can only spread in one dimension below the lithosphere. In particular, no toroidal flow is produced with this geometry. The effect of the resulting planform of convection on the amplitude of the dynamic topography spectrum of our models is difficult to estimate. Moreover, our spectral decomposition of dynamic topography assumes that the statistical distribution of dynamic topography is homogeneous in all directions on a complete sphere. Time-dependent 3-D spherical mantle flow models with an Earth-like Rayleigh number and large radial and lateral viscosity variations are still a computational frontier.

Even though the Rayleigh number, total heat flow and surface plate velocities of our models approach Earth-like values, these models do not fully capture the convective and tectonic behavior of Earth since assumptions and simplifications have been made to solve the problem of time-dependent convection. We do not consider mantle compressibility, which would affect the planform of convection, for computational reasons and not to add further complexity. However, we account for a thermal expansivity decrease with depth, which has the most important contribution on mantle convection planform in the lower mantle and therefore on large-scale dynamic topography (Hansen et al., 1993). Moreover, Steinberger (2016) showed that accounting for compressibility (which depends on both the depth dependence of density and thermal expansivity) does not substantially modify large-scale dynamic topography in instantaneous flow models. Finally, we do

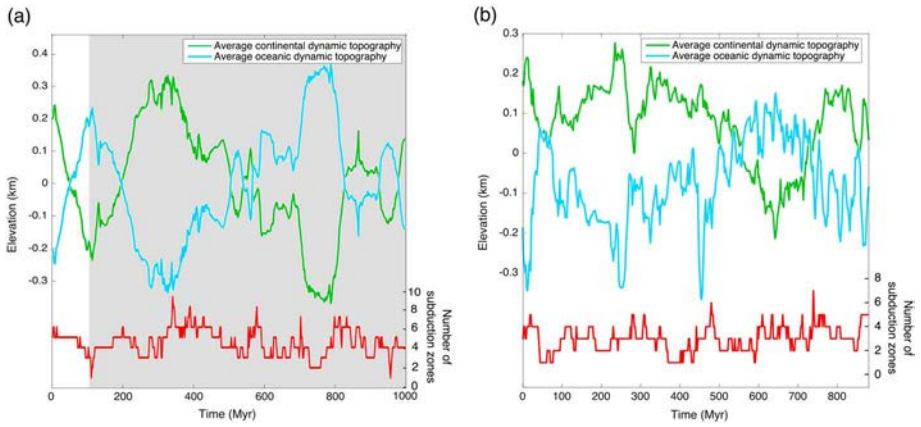

Figure 11. Temporal evolution of average oceanic dynamic topography (blue curve), continental dynamic topography (green curve), and the number of subduction zones in (a) Model 9 and (b) Model 10. The gray-shaded area corresponds to the presence of a supercontinent in Model 9. The average continental dynamic topography evolution compensates the evolution of the average oceanic dynamic topography (the continental and oceanic area are not the same, which explains differences between the blue and green curves). Note the anticorrelation between the evolution of the number of subduction zones and the evolution of average oceanic dynamic topography.

not account for phase transitions in the mantle, which possibly lead to a decrease in the amplitude of surface dynamic topography (Le Stunff & Ricard, 1997).

Our models employ a simplified and empirical rheology (for a review, see Coltice, Gérault, & Ulvrová, 2017), not accounting for the complexity of the coexisting deformation mechanisms at low temperature. Although the use of a power law rheology should improve the plate-like behavior of our models (Bercovici, 2003), Christensen (1984) showed that the convection planform does not differ significantly from that of a diffusion creep law with lower activation energy like in this study. Also, we do not model the elasticity of lithosphere, which would at least partially filter out the shortest wavelengths of dynamic topography (Golle et al., 2012). Considering the elastic properties of the lithosphere would modify the behavior of the highest-frequency surface deflections, depending on the modeled elastic thickness.

We used a free-slip condition at the surface. We thus derived dynamic topography from normal stresses acting on the top boundary, which can produce some artifacts, for example, between continental belts or near subduction trenches. Crameri et al. (2012) showed that the use of a free surface precludes the formation of excessive normal stresses and results in a better resolution of topography. However, this approach drastically increases the computation cost. Moreover, since our surface topography amplitudes are small compared to the domain depth, using the free-slip simplification is still reasonable (Crameri et al., 2012).

4.2. Spatial and Temporal Influence of Dynamic Topography on Surface Processes

The generation of multiple scales of dynamic topography induced by large viscosity contrasts reported herein provides a first step to the modeling of different scales of dynamic topography in 3-D global mantle flow models with plate-like tectonics, and their interplay with surface processes. In the models presented, rapid flow reorganizations occur due to mantle-lithosphere interactions such as the evolution of the spatial distribution of subduction zones, subduction initiation or slab break-offs, changes in slab dip angles, and interaction of small-scale convection and plume heads with the lithosphere. These processes produce dynamic topography over a range of spatial scales that cannot yet be taken into account in 3-D global models because of computational limitations. Our models predict significant intermediate to small scales of dynamic topography, with a spectral distribution similar to the global residual topography spectrum of Hoggard et al. (2016) at spherical harmonic degrees larger than 5 (Figure 7). The dynamic topography spectra that we obtained (Figure 7) are comparable to those derived by recent inversions of present-day mantle structures (Yang & Gurnis, 2016) to simultaneously fit the long-wavelength geoid, free-air gravity anomalies, gravity gradients, and residual topography point data (Hoggard et al., 2016), and of a high-resolution upper mantle tomography model (Steinberger et al., 2017). Nevertheless, we note a significant discrepancy at low spherical harmonic degrees (1–4) between global model dynamic topography spectra, including ours, and the residual topography spectrum of Hoggard et al. (2016), for which power is 10 times lower (Figure 7). The discrepancy between numerical models of dynamic topography and observation-derived present-day dynamic topography remains debated

(e.g., Hoggard et al., 2017, 2016; Molnar et al., 2015; Steinberger et al., 2017; Watkins & Conrad, 2018; Yang & Gurnis, 2016; Yang et al., 2017). Indeed, Hoggard et al., (2016, 2017) proposed from models of residual topography based on seismic profiles in the oceanic realm and free-air gravity anomalies in the continental domain that large-scale dynamic topography has an amplitude of ±300 m at most. More recently, Steinberger et al. (2017) used a crustal model to estimate present-day continental residual topography and also found a limited degree-2 residual topography amplitude. Watkins and Conrad (2018) also inferred a degree-2 residual topography amplitude of about 500 km from the asymmetric subsidence of mid-ocean ridges. However, Yang and Gurnis (2016) and Yang et al. (2017) advocate for low spherical degree of dynamic topography with amplitudes larger than ±1 km, based on a different analysis of residual topography data and consistently with previous numerical models based on seismic tomography or slab assimilation. Our time-dependent models self-generating mantle convective scales with plate-like tectonics and basal chemical heterogeneities support the existence of large-scale dynamic topography of amplitude larger than ±1 km.

Our models predict that the main geodynamic processes controlling the existence of intermediate wavelengths of dynamic topography are associated with plate boundaries, specifically subduction initiation or cessation, while Hoggard et al. (2016) identified intraplate intermediate scales of residual topography and explained them by distributed density anomalies in a fast moving asthenospheric channel. Although our models present large viscosity contrasts between the lithosphere and the asthenosphere, we only observe a significant effect of this low-viscosity layer on dynamic topography at scales smaller than 1,000 km (small-scale convection, Figure 1). It is thought that subduction dynamics control continental sedimentation by favoring regional continental flooding (Mitrovica et al., 1989). In our models, the tilting of continents due to the presence of sinking slabs in the upper mantle can reach 5,000 km in lateral extent (depending on slab geometry), up to 1.5-km amplitude at continental margins and can last up to 50 Myr (Figures 6c and 11). In the case of the tectonic motion of continents over slabs, we observe a propagation of topographic lows toward the center of the continent, reminiscent of the migration of sedimentary depocenters toward the interior of North America (Liu et al., 2008).

Intermediate to long-wavelength dynamic topography variations caused by changes in the planform of convection due to supercontinent cycles or to the evolution of the number of subduction zones (Figure 10) are likely to cause changes in the volume of ocean basins, leading to sea-level changes. For example, Conrad and Husson (2009) studied the effects of continents moving above downwellings, and the effect of Wilson cycles on sea-level variations. They showed that present-day seafloor is uplifted by 132 m (air loaded) due to its preferred position on top on large-scale upwellings while continental areas are deflected by about 295 m because of the presence of dense mantle anomalies below them after the Pangea breakup. They estimated a sea-level rise of 0.44 ± 0.22 m/Myr due to this uplift. Such long-term variations in the seafloor depth occur throughout our models, due to long-term changes in the number of subductions linked with large-scale mantle flow reorganizations. For example, the long-term decrease in the average oceanic dynamic topography between 350 and 750 Myr for Model 9 at a rate of about 1.5 m/Myr (Figure 11a) and between 250 and 650 Myr for Model 10 (Figure 11b) at a rate of about 0.75 m/Myr correspond to the presence of a large-scale upwelling below the oceanic domain, which prevents the initiation of subduction zones in this area at these periods (Figures 6 and 9). Moreover, on Figure 11a, we show that the formation of a supercontinent in Model 9 is associated with a 400-m decrease in the average depth of the seafloor over about 100 Myr (rate of change 4 m/Myr), and that it is compensated by continental deflection over the same period. These amplitudes and rates of change are larger than estimated by Conrad and Husson (2009) and probably result from the 2-D geometry of our models, which leads to higher amplitude and faster motion of the surface since changes in mantle flow are only accommodated along one direction. We therefore show that, in our models, the decrease in the number of subduction zones linked to large-scale reorganizations of mantle flow leads to shallower seafloor, which would increase long-term global sea level.

Faster dynamic topography changes also occur on timescales of 5 Myr to tens of millions of years and can reach up to ±60 m/Myr in average for both oceans and continents (Figures 8c and 11). These are linked with abrupt changes in mantle dynamics, such as the initiation, change in the dip angle or break-off of slabs and the rise of a plume head below the lithosphere. The amounts of vertical stress generated by such events on the lithosphere cause dynamic topography changes with variable amplitude (Figure 11). We expect local stratigraphic sequences with periods as short as ~5 Myr to occur in response to those geodynamic processes. These

intermediate scales of dynamic topography can locally modify shorelines, leading to changes in sedimentation at continental margins such as documented for the North-European margin in the vicinity of the Iceland plume (Hartley et al., 2011).

In our models, dynamic topography is controlled by small-scale convection at wavelengths shorter than 500 km, which is consistent with the study of Petersen et al. (2010) that predicts small-scale dynamic topography (<500 km) with amplitudes of about ±300 m and high-frequency variations (2–20 Myr). Our whole-mantle convection models suggest that small-scale convection induces dynamic topography that would affect sedimentation and continental flooding at spatial scales between 200 and 500 km, with maximal amplitude of ±750 m and period 2–50 Myr. Nevertheless, we observe a partial filtering of small-scale dynamic topography close to continents, which are stiffer and thicker. This could result from an attenuation for dynamic mantle tractions by the lithosphere rheology, as studied in laboratory experiments by Sembroni et al. (2017).

5. Conclusions

We explored the parameter space for convection models in 2-D spherical annulus geometry in which we consider a viscosity jump by a factor of 30 at 660-km depth and an activation energy for the temperature dependence of viscosity of 142 kJ/mol, which leads to a variation of viscosity over 7 orders of magnitude. We identified a range of models in a plate-like tectonic regime with Earth-like surface heat flow, surface velocities, and hypsometric distribution. For these models the Rayleigh number ranges between 1×10^7 and 5×10^7, internal heating rates range between 9×10^{-13} and 1.4×10^{-11} W/kg, and the yield stress ranged between 17 and 49 MPa.

We developed an analytical procedure to compare 2-D spherical annulus power spectra to 3-D spherical harmonic power spectra. The amplitude of large-scale dynamic topography (>10^4 km) varies between −2.1 and +1.4 km in Model 10 (with dense thermochemical piles) and between −3.1 km and +2.3 km in Model 11 (without dense thermochemical piles). In addition, all of these models produce intermediate scales of dynamic topography (500 to 10^4 km — up to degree 30) with a spectral power consistent with those obtained from the study of the residual topography at present day (Hoggard et al., 2016). These models also predict dynamic topography at wavelengths shorter than 500 km.

The longest wavelengths of dynamic topography represent the large-scale convective flow expressed by the large tectonic plates and distribution of lower mantle convective cells. The large-scale flow evolves with continental drift and global tectonic reorganization at timescales >100 Myr. The intermediate scales of dynamic topography correspond to the flow in the upper mantle around subduction zones and depend on the geometry of slabs. In these models, subduction zones last between ten and several hundreds of million years. The shortest scales of dynamic topography are generated by small-scale convection below oceanic and continental lithosphere. In our models, these instabilities evolve rapidly between five and tens of million years.

The parameters we varied influence the distribution of dynamic topography, through the organization of the flow: Increasing the Rayleigh number, decreasing the yield stress, and removing deep dense chemical piles have the similar effect of increasing the number of slabs. In turn, this results in younger ocean floor and in less developed small-scale convection, because small-scale convection preferentially occurs under old seafloor. As a consequence, models with the smallest number of slabs display strong small-scale dynamic topography, and the spectral power of intermediate scales of dynamic topography fluctuates strongly with initiations and break-offs of slabs.

Our models suggest that the flow in the upper mantle, mostly driven by slab evolution over 10–100 Myr generates the intermediate scales of dynamic topography proposed by Hoggard et al. (2016). In the models, these scales occur due to the existence of large lateral viscosity contrasts in the upper mantle. Our models suggest that these intermediate scales coexist with strong large-scale dynamic topography (>10^4 km). We propose that a significant decrease in the number of subduction zones linked with large-scale mantle flow reorganizations, for example related to supercontinent formation, could cause a substantial decrease of the spectral power of intermediate scales of dynamic topography linked with a significant decrease in the average seafloor depth, which would contribute to an increase of sea level and of the area of continental sedimentary basins.

Our study suggests that the interpretation of surface processes, such as sedimentary strata deposition and sea-level change, should consider the effect of dynamic topography at all spatial and temporal scales.

Appendix A: Comparing of a 1-D Discrete Signal With a 2-D Signal Defined on the Sphere $\mathbb{S}^2$

A1. Notations

We consider a real signal $f : \mathbb{S}^2 \longrightarrow \mathbf{R}$. Its spherical harmonic decomposition can be written as

$$f(\theta,\varphi) = \sum_{l=0}^{\infty} \sum_{m=-l}^{l} f_{l,m} Y_{l,m}(\theta,\varphi),$$

where

$$Y_{l,m}(\theta,\varphi) = \overline{P}_{l,m}(\cos(\theta))cos(m\varphi)$$

if $m \geq 0$ and

$$Y_{l,m}(\theta,\varphi) = \overline{P}_{l,|m|}(\cos(\theta))\sin(|m|\varphi)$$

if $m < 0$. We denote by θ the colatitude, by φ the longitude, and by $\overline{P}_{l,m}$ the Legendre polynomials. We note $g_m(\varphi) = \cos(m\varphi)$ if $m \geq 0$ and $g_m(\varphi) = \sin(|m|\varphi)$ if $m < 0$. We use the fully normalized Legendre polynomials:

$$\overline{P}_{l,m}(x) = \sqrt{\frac{(2-\delta_{0,m})(2l+1)}{4\pi}\frac{(l-m)!}{(l+m)!}}P_{l,m}(x),$$

$$P_{l,m}(x) = (1-x^2)^{\frac{m}{2}}\frac{d^m}{dx^m}P_l(x),$$

and

$$P_l(x) = \frac{1}{2^l l!}\frac{d^l}{dx^l}(x^2-1)^l.$$

$(Y_{l,m})_{l\in\mathbb{N},m\in\{-l,\dots,l\}}$ define an orthonormal base for the scalar product $L^2(\mathbb{S}^2, d\Omega)$, with the volume form $d\Omega = |\sin(\theta)|d\theta d\varphi$, where $\theta \in [-\frac{\pi}{2},\frac{\pi}{2}]$ and $\varphi \in [0, 2\pi]$.

A2. Approximation of a Function on a Sphere by Longitudinal Functions

The aim here is to show that we can recover a spherical harmonic spectrum from a function defined on a sphere by summing the Fourier spectra of the same function sampled on a large range of great circles.

Let l be an integer, and ϕ_k a group of longitudes respectively equal to $\frac{2\pi k}{N}$, for a large and fixed N. If $f : \mathbb{S}^2 \longrightarrow \mathbf{R}$ is a function defined on the sphere, we can define the function f_l by

$$f_l(\theta,\varphi) := \sum_{m=-l}^{l} f_{l,m} Y_{l,m}(\theta,\varphi),$$

and for a fixed longitude φ_k, we can define the function f_{l,φ_k} for $\theta \in [-\frac{\pi}{2},\frac{\pi}{2}]$:

$$f_{l,\varphi_k}(\theta) := f_l(\theta,\varphi_k),$$

and for $\theta \in [-\frac{\pi}{2},\frac{3\pi}{2}]$:

$$f_{l,\varphi_k}(\theta) := f_l(-\theta+\pi,\pi+\varphi_k)$$

We can extend f_{l,φ_k} to a 2π-periodic function, simply representing the function f_l restricted to the two half great circles defined by the longitudes φ_k and $\varphi_{k+\frac{N}{2}}$.

We can define, for $j \neq 0$:

$$a_{(l,m),(j,k)} = \frac{1}{\pi}\int_0^{2\pi} Y_{l,m,\varphi_k}(\theta)\sqrt{|\sin(\theta)|}\cos(j\theta)d\theta$$

and

$$b_{(l,m),(j,k)} = \frac{1}{\pi}\int_0^{2\pi} Y_{l,m,\varphi_k}(\theta)\sqrt{|\sin(\theta)|}\sin(j\theta)d\theta,$$

and for $j = 0$:

$$a_{(l,m),(0,k)} = \frac{1}{2\pi}\int_0^{2\pi} Y_{l,m,\varphi_k}(\theta)\sqrt{|\sin(\theta)|}d\theta$$

and

$$b_{(l,m),(0,k)} = 0,$$

the real Fourier coefficients of the θ-dependent function given by $Y_{l,\varphi_k}(\theta)\sqrt{|\sin(\theta)|}$.

The separation of the variables θ and φ in the expression of $Y_{l,m}(\theta,\phi)$ leads to, for any j, k, and l,

$$a_{l,(j,k)} = \sum_{m=-l}^{l} g_m(\varphi_k)\frac{2-\delta_{0,j}}{2\pi}\int_0^{2\pi}\overline{P}_{l,m}(\cos(\theta))\sqrt{|\sin(\theta)|}\cos(j\theta)\mathrm{d}\theta$$

and to

$$b_{l,(j,k)} = \sum_{m=-l}^{l} g_m(\varphi_k)\frac{1}{\pi}\int_0^{2\pi}\overline{P}_{l,m}(\cos(\theta))\sqrt{|\sin(\theta)|}\sin(j\theta)\mathrm{d}\theta.$$

Let $\alpha_{j,(l,m)}$ be the Fourier coefficient,

$$\alpha_{j,(l,m)} := \frac{2-\delta_{0,j}}{2\pi}\int_0^{2\pi}\overline{P}_{l,m}(\cos(\theta))\sqrt{|\sin(\theta)|}\cos(j\theta)\mathrm{d}\theta,$$

and $\beta_{j,(l,m)}$ the coefficient,

$$\beta_{j,(l,m)} := \frac{1}{\pi}\int_0^{2\pi}\overline{P}_{l,m}(\cos(\theta))\sqrt{|\sin(\theta)|}\sin(j\theta)\mathrm{d}\theta.$$

We want to compare the spherical harmonic power spectrum of f_l given by $S(f_l) = \sum_{m=-l}^{l} f_{l,m}^2$ (with the chosen normalization conventions), and the k averaged from 0 to $\frac{N}{2}$ of the Fourier power spectrum of $f_{l,\varphi_k}(\theta)\sqrt{|\sin(\theta)|}$.

Therefore, we consider the sum over each k:

$$s_k(f)(\theta) := \sum_{j=0}^{\infty}\sum_{m=-l}^{l} f_{l,m}(a_{j,k}\cos(j\theta) + b_{j,k}\sin(j\theta))$$

for which we want to calculate the spectral power. Its Fourier coefficients are $\sum_{m=-l}^{l} f_{l,m}a_{j,k}$ and $\sum_{m=-l}^{l} b_{j,k}f_{l,m}$.

Parseval's identity gives

$$\frac{1}{2\pi}\int_0^{2\pi} s_k(f)(\theta)^2\mathrm{d}\theta = \left(\sum_{m=-l}^{l} f_{l,m}a_{0,k}\right)^2 + \frac{1}{2}\sum_{j=0}^{\infty}\left(\left(\sum_{m=-l}^{l} f_{l,m}a_{j,k}\right)^2 + \left(\sum_{m=-l}^{l} f_{l,m}b_{j,k}\right)^2\right).$$

We name this expression $P_F(s_k(f))$. Let us consider the first sum of the second member of this identity. By taking its square and its average over k, we get

$$\begin{aligned}\frac{2}{N}\sum_{k=0}^{\frac{N}{2}-1}\sum_{m=-l}^{l}\sum_{m'=-l}^{l} f_{l,m}f_{l,m'}a_{0,k}^2 &= \sum_{m=-l}^{l}\sum_{m'=-l}^{l} f_{l,m}f_{l,m'}\frac{2}{N}\sum_{k=0}^{\frac{N}{2}-1} a_{0,k}^2 \\ &= \sum_{m=-l}^{l}\sum_{m'=-l}^{l} f_{l,m}f_{l,m'}\alpha_{0,(l,m)}\alpha_{0,(l,m')}\frac{2}{N}\sum_{k=0}^{\frac{N}{2}-1} g_m(\varphi_k)g_{m'}(\varphi_k).\end{aligned}$$

This last equation contains a Riemann sum for each m, for which the convergence rate only depends on m and thus on l. We therefore have

$$\frac{2}{N}\sum_{k=0}^{\frac{N}{2}-1} g_m(\varphi_k)g_{m'}(\varphi_k) = \frac{2}{N}\sum_{k=0}^{\frac{N}{2}-1} g_m(\pi k\frac{2}{N})g_{m'}(\pi k\frac{2}{N}),$$

For a large N, this gives

$$\frac{2}{N}\sum_{k=0}^{\frac{N}{2}-1} g_m(\varphi_k)g_{m'}(\varphi_k) \approx \int_0^1 g_m(\pi t)g_{m'}(\pi t)\mathrm{d}t$$

(We can replace the "≈" sign by an "=" sign only if N tends to infinity.) After a simple calculation, this gives

$$\frac{2}{N}\sum_{k=0}^{\frac{N}{2}-1} g_m(\varphi_k)g_{m'}(\varphi_k) \approx \delta_{m,m'}\int_0^1 g_m(\pi t)^2\mathrm{d}t.$$

We recall that $g_m(\pi t)^2$ is equal to $\cos(m\pi t)^2$ for any positive m and to $\sin(m\pi t)^2$ for any negative m. We therefore have, for any $m \neq 0$:

$$\int_0^1 g_m(\pi t)^2 \mathrm{d}t = \frac{1}{2}$$

and

$$\int_0^1 g_0(\pi t)^2 \mathrm{d}t = 1.$$

The sum over m and m' then leads to

$$\sum_{m=-l}^{l} \sum_{m'=-l}^{l} f_{l,m} f_{l,m'} \alpha_{0,(l,m)} \alpha_{0,(l,m')} \frac{2}{N} \sum_{k=0}^{\frac{N}{2}-1} g_m(\varphi_k) g_{m'}(\varphi_k) \approx \sum_{m=0}^{l} \alpha_{0,(l,m)}^2 \frac{1}{2} (f_{l,m}^2 + f_{l,-m}^2).$$

The approximation is valid because the rate of convergence only depends on l.

We can do the same calculations for any j. We then get, for any $j \geq 1$,

$$\frac{2}{N} \sum_{k=0}^{\frac{N}{2}-1} \left(\sum_{m=-l}^{l} f_{l,m} a_{j,k} \right)^2 \approx \sum_{m=0}^{l} \alpha_{j,(l,m)}^2 \frac{1}{2} (f_{l,m}^2 + f_{l,-m}^2)$$

and

$$\frac{2}{N} \sum_{k=0}^{\frac{N}{2}-1} \left(\sum_{m=-l}^{l} f_{l,m} b_{j,k} \right)^2 \approx \sum_{m=0}^{l} \beta_{j,(l,m)}^2 \frac{1}{2} (f_{l,m}^2 + f_{l,-m}^2).$$

Finally, this leads to

$$\frac{2}{N} \sum_{k=0}^{\frac{N}{2}-1} P_F(s_k(f)) \approx$$
$$\sum_{m=0}^{l} \alpha_{0,(l,m)}^2 \frac{1}{2} \left(f_{l,m}^2 + f_{l,-m}^2 \right) + \frac{1}{2} \sum_{j=1}^{\infty} \left(\sum_{m=0}^{l} \alpha_{j,(l,m)}^2 \frac{1}{2} \left(f_{l,m}^2 + f_{l,-m}^2 \right) + \sum_{m=0}^{l} \beta_{j,(l,m)}^2 \frac{1}{2} \left(f_{l,m}^2 + f_{l,-m}^2 \right) \right).$$

By inverting the two sums, we have

$$\frac{2}{N} \sum_{k=0}^{\frac{N}{2}-1} P_F(s_k(f)) \approx \sum_{m=0}^{l} \frac{1}{2} \left(f_{l,m}^2 + f_{l,-m}^2 \right) \left(\alpha_{0,(l,m)}^2 + \frac{1}{2} \sum_{j=1}^{\infty} \alpha_{j,(l,m)}^2 + \beta_{j,(l,m)}^2 \right).$$

The sum over j contains the Fourier development of $\overline{P}_{l,m}(\cos(\theta)\sqrt{|\sin(\theta)|}$. Thanks to the Parseval's identity, we know that this sum equals to

$$\frac{1}{2\pi} \int_{-\pi}^{\pi} \overline{P}_{l,m}(\cos(\theta))^2 |\sin(\theta)| \mathrm{d}\theta.$$

The change of variables $u = \cos(\theta)$ leads to

$$\frac{1}{\pi} \int_{-1}^{1} \overline{P}_{l,m}(u)^2 \mathrm{d}u,$$

which is equal to $\frac{2(2-\delta_{0,m})}{4\pi^2}$.

Finally, we get, by dividing the sum with the part of negative m:

$$\frac{2}{N} \sum_{k=0}^{\frac{N}{2}-1} P_F(s_k(f)) \approx \frac{1}{2\pi^2} \sum_{m=-l}^{l} f_{l,m}^2.$$

Therefore,

$$\frac{2}{N} \sum_{k=0}^{\frac{N}{2}-1} \int_0^{2\pi} s_k(f)(\theta)^2 \mathrm{d}\theta \approx \frac{1}{\pi} \times S(f_l).$$

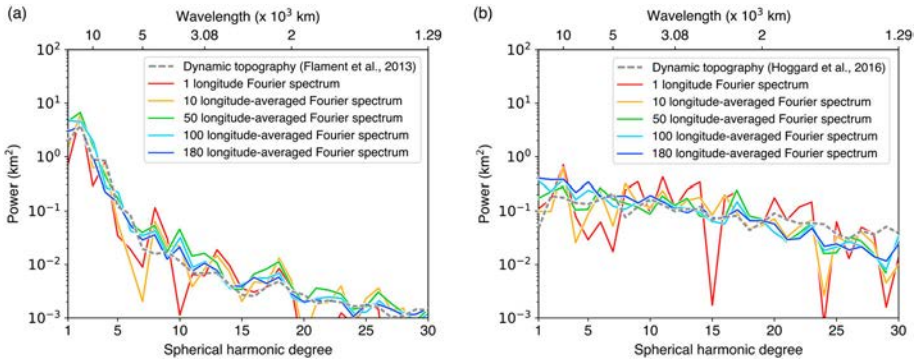

Figure A1. Comparison of the spherical harmonic spectrum of dynamic topography from (a) Flament et al. (2013) and (b) Hoggard et al. (2016) with the longitudinal average of the Fourier power spectra of dynamic topography by Flament et al. (2013) and Hoggard et al. (2016), respectively, sampled over 1, 10, 50, 100, and 180 longitudinal great circles.

In conclusion, in order to retrieve the spherical harmonic power of a 2-D signal f_l defined on the sphere $\mathbb{S}^2$ from Fourier power spectra of the same signal f_{l,φ_k} restricted to two half great circles defined by the longitudes φ_k and $\varphi_{k+\frac{N}{2}}$, we need to consider the sum over a large range N of longitudes of the Fourier spectral power coefficients of the following function $f_{l,\varphi_k}\sqrt{|\sin(\theta)|}$, then divided by $\frac{1}{\pi}$.

We applied this method to the dynamic topography field of Flament et al. (2013). We decomposed this field into 180 signals defined on longitudinal great circles. We then calculated their corresponding Fourier spectra accordingly to the method described before. We averaged the resulting power spectral coefficients of all great circles for each frequency k and compared the resulting spectrum with the known spherical harmonic spectrum of the whole field (Figure A1).

From Figure A1a, we show that we successfully recover the spherical harmonic power spectrum of Flament et al. (2013) by using the method described before. The two curves are not exactly superposed because we only averaged Fourier spectra over 180 great circles. However, the method described before is exact for an infinite number of signals restricted to longitudinal great circles.

We repeated the same process for different dynamic topography global fields (Conrad & Husson, 2009; Steinberger, 2007; Ricard et al., 1993; Spasojevic & Gurnis, 2012) and Yang and Gurnis (2016), with the same positive conclusions. The same process applied to the residual topography field of Hoggard et al. (2016), which has more signal in the small wavelengths reveals that the recovery of the initial signal is consistent but not fully complete: The spectral power of the largest scales of dynamic topography (degrees >6) is slightly overestimated by about 0.3 km^2, while the power at degrees <20 is slightly underestimated by about 0.05 km^2.

When we calculate dynamic topography power spectra for our models, we repeat the procedure described above and add a correction of the slope of the Fourier power spectra by dividing the amplitude of each spherical harmonic degree l by $2l + 1$ to account for the degree-dependent slope of spherical harmonics decomposition (Maus, 2001).

Acknowledgments
We thank Mark Hoggard, an anonymous referee and the Associate Editor for their constructive reviews. The data used are listed in the references, tables, and Appendix. We thank S. Durand for sharing data used in Figure 4. The research leading to these results has received funding from the European Research Council within the framework of the SP2-Ideas Program ERC-2013-CoG, under ERC grant agreement 617588. Calculations were performed on the Augury supercomputer at P2CHPD Lyon and with the assistance of resources from the National Computational Infrastructure (NCI), which is supported by the Australian Government. M. A. benefited from funding provided by the grant 15.007742.01 from Région Rhône-Alpes and a grant from Programme Avenir Lyon Saint-Etienne. N. F. was supported by ARC DE160101020. R. D. M. was supported by ARC IH130200012.

References

Al-Hajri, Y., White, N., & Fishwick, S. (2009). Scales of transient convective support beneath Africa. *Geology*, *37*(10), 883–886.
Allmann, B. P., & Shearer, P. M. (2009). Global variations of stress drop for moderate to large earthquakes. *Journal of Geophysical Research*, *114*, B01310. https://doi.org/10.1029/2008JB005821
Amante, C., & Eakins, B. W. (2009). ETOPO1 1 arc-minute global relief model: Procedures, data sources and analysis. US Department of Commerce, National Oceanic and Atmospheric Administration, National Environmental Satellite, Data, and Information Service, National Geophysical Data Center, Marine Geology and Geophysics Division Colorado https://doi.org/10.1594/PANGAEA.769615
Ballmer, M. D., Ito, G., Van Hunen, J., & Tackley, P. J. (2011). Spatial and temporal variability in Hawaiian hotspot volcanism induced by small-scale convection. *Nature Geoscience*, *4*(7), 457.
Bercovici, D. (2003). The generation of plate tectonics from mantle convection. *Earth and Planetary Science Letters*, *205*(3-4), 107–121.
Bower, D. J., Gurnis, M., & Flament, N. (2015). Assimilating lithosphere and slab history in 4-D Earth models. *Physics of the Earth and Planetary Interiors*, *238*, 8–22.
Brace, W., & Kohlstedt, D. (1980). Limits on lithospheric stress imposed by laboratory experiments. *Journal of Geophysical Research*, *85*(B11), 6248–6252. https://doi.org/10.1029/JB085iB11p06248
Butterworth, S. (1930). On the theory of filter amplifiers. *Wireless Engineer*, *7*(6), 536–541.
Chopelas, A., & Boehler, R. (1992). Thermal expansivity in the lower mantle. *Geophysical Research Letters*, *19*(19), 1983–1986. https://doi.org/10.1029/92GL02144

Christensen, U. (1984). Convection with pressure- and temperature-dependent non-Newtonian rheology. *Geophysical Journal International*, *77*(2), 343–384.
Coltice, N., Gérault, M., & Ulvrová, M. (2017). A mantle convection perspective on global tectonics. *Earth-Science Reviews*, *165*, 120–150. https://doi.org/10.1016/j.earscirev.2016.11.006
Coltice, N., Larrouturou, G., Debayle, E., & Garnero, E. J. (2017). Interactions of scales of convection in the Earth's mantle. *Tectonophysics*. https://doi.org/10.1016/j.tecto.2017.06.028
Coltice, N., Rolf, T., Tackley, P., & Labrosse, S. (2012). Dynamic causes of the relation between area and age of the ocean floor. *Science*, *336*(6079), 335–338.
Conrad, C. P., & Gurnis, M. (2003). Seismic tomography, surface uplift, and the breakup of Gondwanaland: Integrating mantle convection backwards in time. *Geochemistry, Geophysics, Geosystems*, *4*(3), 1031. https://doi.org/0.1029/2001GC000299
Conrad, C. P., & Husson, L. (2009). Influence of dynamic topography on sea level and its rate of change. *Lithosphere*, *1*(2), 110–120. https://doi.org/10.1130/L32.1
Crameri, F., Schmeling, H., Golabek, G., Duretz, T., Orendt, R., Buiter, S., et al. (2012). A comparison of numerical surface topography calculations in geodynamic modelling: An evaluation of the 'sticky air' method. *Geophysical Journal International*, *189*(1), 38–54. https://doi.org.10.1111/j.1365-246X.2012.05388.x
Czarnota, K., Hoggard, M., White, N., & Winterbourne, J. (2013). Spatial and temporal patterns of cenozoic dynamic topography around Australia. *Geochemistry, Geophysics, Geosystems*, *14*, 634–658.
Davaille, A., Le Bars, M., & Carbonne, C. (2003). Thermal convection in a heterogeneous mantle. *Comptes Rendus Geoscience*, *335*(1), 141–156. https://doi.org/10.1016/S1631-0713(03)00003-8
Deschamps, F., & Tackley, P. J. (2009). Searching for models of thermo-chemical convection that explain probabilistic tomography. II—Influence of physical and compositional parameters. *Physics of the Earth and Planetary Interiors*, *176*(1), 1–18. https://doi.org/10.1016/j.pepi.2009.03.012
Flament, N., Gurnis, M., & Müller, R. D. (2013). A review of observations and models of dynamic topography. *Lithosphere*, *5*(2), 189–210. https://doi.org/10.1130/L245.1
Flament, N., Gurnis, M., Müller, R. D., Bower, D. J., & Husson, L. (2015). Influence of subduction history on South American topography. *Earth and Planetary Science Letters*, *430*, 9–18.
Garnero, E. J., McNamara, A. K., & Shim, S.-H. (2016). Continent-sized anomalous zones with low seismic velocity at the base of Earth's mantle. *Nature Geoscience*, *9*, 481–489. https://doi.org/10.1038/ngeo2733
Gillet, P., Daniel, I., Guyot, F., Matas, J., & Chervin, J.-C. (2000). A thermodynamic model for $MgSiO_3$-perovskite derived from pressure, temperature and volume dependence of the Raman mode frequencies. *Physics of the Earth and Planetary Interiors*, *117*(1), 361–384. https://doi.org/10.1016/S0031-9201(99)00107-7
Golle, O., Dumoulin, C., Choblet, G., & Cadek, O. (2012). Topography and geoid induced by a convecting mantle beneath an elastic lithosphere,. *Geophysical Journal International*, *189*(1), 55–72. https://doi.org/10.1111/j.1365-246X.2012.05364.x
Gurnis, M. (1993). Phanerozoic marine inundation of continents driven by dynamic topography above subducting slabs. *Nature*, *364*(6438), 589–593. https://doi.org/10.1038/364589a0
Gvirtzman, Z., Faccenna, C., & Becker, T. W. (2016). Isostasy, flexure, and dynamic topography. *Tectonophysics*, *683*, 255–271. https://doi.org/10.1016/j.tecto.2016.05.041
Hager, B. H., Clayton, R. W., Richards, M. A., Comer, R. P., & Dziewonski, A. M. (1985). Lower mantle heterogeneity, dynamic topography and the geoid. *Nature*, *313*(6003), 541–545.
Hager, B., & Richards, M. (1989). Long-wavelength variations in Earth's geoid: Physical models and dynamical implications. *Philosophical Transactions of the Royal Society of London A: Mathematical, Physical and Engineering Sciences*, *328*(1599), 309–327. https://doi.org/10.1098/rsta.1989.0038
Hansen, U., Yuen, D., Kroening, S., & Larsen, T. (1993). Dynamical consequences of depth-dependent thermal expansivity and viscosity on mantle circulations and thermal structure. *Physics of the earth and planetary interiors*, *77*(3), 205–223. https://doi.org/10.1016/0031-9201(93)90099-U
Hartley, R. A., Roberts, G. G., White, N., & Richardson, C. (2011). Transient convective uplift of an ancient buried landscape. *Nature Geoscience*, *4*(8), 562–565. https://doi.org/10.1038/NGEO1191
Haxby, W. F., & Weissel, J. K. (1986). Evidence for small-scale mantle convection from SEASAT altimeter data. *Journal of Geophysical Research*, *91*(B3), 3507–3520. https://doi.org/10.1029/JB091iB03p03507
Hernlund, J. W., & Tackley, P. J. (2008). Modeling mantle convection in the spherical annulus. *Physics of the Earth and Planetary Interiors*, *171*(1), 48–54. https://doi.org/10.1098/rsta.1989.0038
Hirth, G., & Kohlstedt, D. (2003). Rheology of the upper mantle and the mantle wedge: A view from the experimentalists. *Inside the subduction Factory*, *138*, 83–105.
Hoggard, M., White, N., & Al-Attar, D. (2016). Global dynamic topography observations reveal limited influence of large-scale mantle flow. *Nature Geoscience*, *9*, 456–463. https://doi.org/10.1038/NGEO2709
Hoggard, M. J., Winterbourne, J., Czarnota, K., & White, N. (2017). Oceanic residual depth measurements, the plate cooling model, and global dynamic topography. *Journal of Geophysical Research: Solid Earth*, *122*, 2328–2372. https://doi.org/10.1002/2016JB013457
Huang, J., Zhong, S., & van Hunen, J. (2003). Controls on sublithospheric small-scale convection. *Journal of Geophysical Research*, *108*(B8), 2405. https://doi.org/10.1029/2003JB002456
Husson, L., Guillaume, B., Funiciello, F., Faccenna, C., & Royden, L. H. (2012). Unraveling topography around subduction zones from laboratory models. *Tectonophysics*, *526*, 5–15. https://doi.org/10.1016/j.tecto.2011.09.001
Jaupart, C., Labrosse, S., & Mareschal, J. (2007). 7.06 Temperatures, heat and energy in the mantle of the Earth. *Treatise on geophysics*, *7*, 223–270.
King, S. D. (2009). On topography and geoid from 2-D stagnant lid convection calculations. *Geochemistry, Geophysics, Geosystems*, *10*, Q03002. https://doi.org/10.1029/2008GC002250
Kreemer, C., Blewitt, G., & Klein, E. C. (2014). A geodetic plate motion and global strain rate model. *Geochemistry, Geophysics, Geosystems*, *15*, 3849–3889. https://doi.org/10.1002/2014GC005407
Le Stunff, Y., & Ricard, Y. (1997). Partial advection of equidensity surfaces: A solution for the dynamic topography problem? *Journal of Geophysical Research*, *102*(B11), 24,655–24,667.
Lenardic, A., & Moresi, L.-N. (1999). Some thoughts on the stability of cratonic lithosphere: Effects of buoyancy and viscosity. *Journal of Geophysical Research*, *104*(B6), 12,747–12,758. https://doi.org/10.1029/1999JB900035
Lithgow-Bertelloni, C., & Silver, P. G. (1998). Dynamic topography, plate driving forces and the African superswell. *Nature*, *395*(6699), 269–272. https://doi.org/10.1038/26212

Liu, L., Spasojević, S., & Gurnis, M. (2008). Reconstructing Farallon plate subduction beneath North America back to the Late Cretaceous. *Science*, *322*(5903), 934–938.
Mallard, C., Coltice, N., Seton, M., Müller, R. D., & Tackley, P. J. (2016). Subduction controls the distribution and fragmentation of Earth's tectonic plates. *Nature*, *535*, 140–143.
Maus, S (2001). New statistical methods in gravity and magnetics.
Mitrovica, J., Beaumont, C., & Jarvis, G. (1989). Tilting of continental interiors by the dynamical effects of subduction. *Tectonics*, *8*(5), 1079–1094. https://doi.org/10.1029/TC008i005p01079
Molnar, P., England, P. C., & Jones, C. H. (2015). Mantle dynamics, isostasy, and the support of high terrain. *Journal of Geophysical Research: Solid Earth*, *120*, 1932–1957. https://doi.org/10.1002/2014JB011724
Moresi, L.-N., & Solomatov, V. (1995). Numerical investigation of 2D convection with extremely large viscosity variations. *Physics of Fluids*, *7*(9), 2154–2162. https://doi.org/10.1063/1.868465
Nakiboglu, S., & Lambeck, K. (1980). Deglaciation effects on the rotation of the Earth. *Geophysical Journal International*, *62*(1), 49–58. https://doi.org/10.1111/j.1365-246X.1980.tb04843.x
Olson, P. (2016). Mantle control of the geodynamo: Consequences of top-down regulation. *Geochemistry, Geophysics, Geosystems*, *17*, 1935–1956. https://doi.org/10.1002/2016GC006334
Pekeris, C. L. (1935). Thermal convection in the interior of the Earth. *Geophysical Journal International*, *3*(8), 343–367. https://doi.org/10.1111/j.1365-246X.1935.tb01742.x
Petersen, K. D., Nielsen, S., Clausen, O., Stephenson, R., & Gerya, T. (2010). Small-scale mantle convection produces stratigraphic sequences in sedimentary basins. *Science*, *329*(5993), 827–830. https://doi.org/10.1126/science.1190115
Pritchard, D., Roberts, G., White, N., & Richardson, C. (2009). Uplift histories from river profiles. *Geophysical Research Letters*, *36*, L24301. https://doi.org/10.1029/2009GL040928
Ricard, Y. (2015). Physics of mantle convection. *Treatise of Geophysics*, *7*, 23–71.
Ricard, Y., Richards, M., Lithgow-Bertelloni, C., & Le Stunff, Y. (1993). A geodynamic model of mantle density heterogeneity. *Journal of Geophysical Research*, *98*(B12), 21,895–21,909. https://doi.org/10.1029/93JB02216
Ritsema, J., Deuss, A., Van Heijst, H., & Woodhouse, J. (2011). S40rts: A degree-40 shear-velocity model for the mantle from new Rayleigh wave dispersion, teleseismic traveltime and normal-mode splitting function measurements. *Geophysical Journal International*, *184*(3), 1223–1236. https://doi.org/10.1111/j.1365-246X.2010.04884.x
Roberts, G. G., Paul, J. D., White, N., & Winterbourne, J. (2012). Temporal and spatial evolution of dynamic support from river profiles: A framework for Madagascar. *Geochemistry, Geophysics, Geosystems*, *13*, Q04004. https://doi.org/10.1029/2012GC004040
Rowley, D. B., Forte, A. M., Moucha, R., Mitrovica, J. X., Simmons, N. A., & Grand, S. P. (2013). Dynamic topography change of the eastern United States since 3 million years ago. *Science*, *340*(6140), 1560–1563.
Sembroni, A., Kiraly, A., Faccenna, C., Funiciello, F., Becker, T. W., Globig, J., & Fernandez, M. (2017). Impact of the lithosphere on dynamic topography: Insights from analogue modeling. *Geophysical Research Letters*, *44*, 2693–2702. https://doi.org/10.1002/2017GL072668
Solomatov, V., & Moresi, L.-N. (2000). Scaling of time-dependent stagnant lid convection: Application to small-scale convection on Earth and other terrestrial planets. *Journal of Geophysical Research*, *105*(B9), 21,795–21,817.
Sotin, C., & Labrosse, S. (1999). Three-dimensional thermal convection in an iso-viscous, infinite prandtl number fluid heated from within and from below: Applications to the transfer of heat through planetary mantles. *Physics of the Earth and Planetary Interiors*, *112*(3-4), 171–190.
Spasojevic, S., & Gurnis, M. (2012). Sea level and vertical motion of continents from dynamic earth models since the Late Cretaceous. *AAPG bulletin*, *96*(11), 2037–2064. https://doi.org/10.1306/03261211121
Steinberger, B. (2007). Effects of latent heat release at phase boundaries on flow in the Earth's mantle, phase boundary topography and dynamic topography at the Earth's surface. *Physics of the Earth and Planetary Interiors*, *164*(1), 2–20. https://doi.org/10.1016/j.pepi.2007.04.021
Steinberger, B. (2016). Topography caused by mantle density variations: Observation-based estimates and models derived from tomography and lithosphere thickness. *Geophysical Supplements to the Monthly Notices of the Royal Astronomical Society*, *205*(1), 604–621.
Steinberger, B., Conrad, C. P., Tutu, A. O., & Hoggard, M. J. (2017). On the amplitude of dynamic topography at spherical harmonic degree two. *Tectonophysics*. https://doi.org/10.1016/j.tecto.2017.11.032
Tackley, P. J. (2000). Self-consistent generation of tectonic plates in time-dependent, three-dimensional mantle convection simulations. *Geochemistry, Geophysics, Geosystems*, *1*(8), 1026–1039. https://doi.org/10.1029/2000GC000036
Tackley, P. J., & King, S. D. (2003). Testing the tracer ratio method for modeling active compositional fields in mantle convection simulations. *Geochemistry, Geophysics, Geosystems*, *4*(4), 8302. https://doi.org/10.1029/2001GC000214
Tosi, N., Yuen, D. A., de Koker, N., & Wentzcovitch, R. M. (2013). Mantle dynamics with pressure-and temperature-dependent thermal expansivity and conductivity. *Physics of the Earth and Planetary Interiors*, *217*, 48–58. https://doi.org/10.1016/j.pepi.2013.02.004
Turcotte, D., & Schubert, G. (2014). *Geodynamics*: Cambridge University Press.
Watkins, C. E., & Conrad, C. P. (2018). Constraints on dynamic topography from asymmetric subsidence of the mid-ocean ridges. *Earth and Planetary Science Letters*, *484*, 264–275.
Yang, T., & Gurnis, M. (2016). Dynamic topography, gravity and the role of lateral viscosity variations from inversion of global mantle flow. *Geophysical Journal International*, *207*(2), 1186–1202. https://doi.org/10.1093/gji/ggw335
Yang, T., Moresi, L., Müller, R. D., & Gurnis, M. (2017). Oceanic residual topography agrees with mantle flow predictions at long wavelengths. *Geophysical Research Letters*, *44*(21), 10,896–10,906. https://doi.org/10.1002/2017GL074800